

www.acsami.org Research Article

Tailoring 3D-Printed Electrodes for Enhanced Water Splitting

Raúl A. Márquez, Kenta Kawashima, Yoon Jun Son, Roger Rose, Lettie A. Smith, Nathaniel Miller, Omar Ali Carrasco Jaim, Hugo Celio, and C. Buddie Mullins*



Cite This: ACS Appl. Mater. Interfaces 2022, 14, 42153–42170



ACCESS I

III Metrics & More

Article Recommendations

Supporting Information

ABSTRACT: Alkaline water electrolysis, a promising technology for clean energy storage, is constrained by extrinsic factors in addition to intrinsic electrocatalytic activity. To begin to compare between catalytic materials for electrolysis applications, these extrinsic factors must first be understood and controlled. Here, we modify extrinsic electrode properties and study the effects of bubble release to examine how the electrode and surface design impact the performance of water electrolysis. We fabricate robust and cost-effective electrodes through a sequential three-dimensional (3D) printing and metal deposition procedure. Through a systematic assessment of the deposition procedure, we confirm the close relationship between extrinsic



electrode properties (*i.e.*, wettability, surface roughness, and electrochemically active surface area) and electrochemical performance. Modifying the electrode geometry, size, and electrolyte flow rate results in an overpotential decrease and different bubble diameters and lifetimes for the hydrogen (HER) and oxygen evolution reactions (OER). Hence, we demonstrate the essential role of the electrode architecture and forced electrolyte convection on bubble release. Additionally, we confirm the suitability of ordered, Nicoated 3D porous structures by evaluating the HER/OER performance, bubble dissipation, and long-term stability. Finally, we utilize the 3D porous electrode as a support for studying a benchmark NiFe electrocatalyst, confirming the robustness and effectiveness of 3D-printed electrodes for testing electrocatalytic materials while extrinsic properties are precisely controlled. Overall, we demonstrate that tailoring electrode architectures and surface properties result in precise tuning of extrinsic electrode properties, providing more reproducible and comparable conditions for testing the efficiency of electrode materials for water electrolysis.

KEYWORDS: 3D printing, water splitting, gas bubbles, electrocatalyst, electrodeposition

1. INTRODUCTION

Increased energy consumption has led to a surge of CO2 and other gases (e.g., SO_x , NO_x) in the atmosphere, exacerbating climate change and environmental pollution that inevitably lead to adverse health effects on society. To circumvent fossil fuel consumption and its consequences, an energy economy built on water electrolysis, using hydrogen (H₂) and electricity as primary energy carriers, offers an alternative for grid-scale energy storage. Water electrolysis relies on electricity to split water into hydrogen and oxygen in a device known as an electrolyzer. An electrolyzer is composed of two electrodes, a cathode, where the hydrogen evolution reaction (HER) occurs, and an anode, where the oxygen evolution reaction (OER) occurs. This reaction initiates at a theoretical cell voltage of 1.23 V in practice; however, higher potentials (i.e., overpotential) must be applied to overcome kinetic barriers. Among currently available electrolysis technologies, alkaline water electrolysis is considered the most advanced and inexpensive option with efficiencies up to 60%, which can be obtained at a cost of \sim \$5.5 kg⁻¹ H₂. Still, these technologies need to overcome significant challenges to be competitive with current technologies (e.g., steam-CH₄ reforming, \$1.5 kg⁻¹ H₂). Improvements must be made to surpass intrinsic energetic barriers, improve stability, and reduce operation costs.

Aside from efforts to increase the intrinsic activity using novel electrocatalysts, improving the performance of water electrolyzers by controlling extrinsic properties (i.e., those independent of the electrode material, including the electrode shape and geometry, surface roughness, wettability, and surface area) is essential for increasing electrolyzer efficiency. Extrinsic properties bring about critical challenges during water electrolysis, mainly due to their impact on the formation of gas bubbles that increase the ohmic interelectrode resistance and block the active surface area of the catalyst, resulting in decreased electrolyzer performance, especially at practical current densities (>1 Acm⁻²).⁶⁻⁹ Given these limitations, previous studies have explored controlling different extrinsic properties for improved water electrolysis performance. For instance, it has been shown that increasing the hydrophilicity and surface roughness of electrocatalyst results in lower overpotentials and improved

Received: July 14, 2022 Accepted: September 1, 2022 Published: September 9, 2022





bubble release. 10,11 Furthermore, constructing ordered electrode architectures with augmented wettability and large surface area has resulted in enhanced bubble release.^{7,12} Yang et al. examined the impact of geometric properties such as the surface area and pore size of Ni-based microstructured porous electrodes, leading to the effective removal of bubbles and delivering high current densities (25 A·cm⁻²) for over 100 h.⁷ Similar studies have found that three-dimensional (3D) macrostructures with large specific surface areas can effectively disperse bubbles, serving as ideal electrode substrates for the HER and OER. 13-15 Hence, understanding how extrinsic properties define the electrochemical performance and formation of bubbles is essential for improving water electrolysis.

Furthermore, ordered electrode structures with tailored geometries have been used to precisely characterize the relationship between electrode structure and electrochemical performance.^{6,9} However, fabrication of complex electrode geometries is challenging via conventional methods. 16 3D printing has been utilized to circumvent this challenge and rapidly prototype complex and tailored designs with unique chemical and structural features. ^{17–21} Kou et al. found that 3Dprinted electrodes with ordered and periodic lattices suppressed bubble trapping and provided uniform flow compared to commercial nickel foam (NF) electrodes. Also, Paul et al. demonstrated that patterning Ni surfaces with uniform arrays of cylindrical recesses and pillars through photolithographic techniques resulted in higher current densities relative to planar Ni electrodes.²² Furthermore, our group has achieved more reproducible testing conditions compared to traditional threeelectrode cells due to 3D-printed electrolyzers that enhance mass transport and electrolyte mixing. 23,24 Therefore, using architectures with precise electrolyzer designs also enables a controlled environment for studying the activity of electrocatalytic materials for water splitting while enabling high reproducibility. However, despite the variety of architectures reported in the literature, it is still uncertain how electrodes should be designed to systematically reduce the impact of extrinsic properties and provide more reproducible measure-

Here, we document the impact of extrinsic electrode properties on the electrochemical performance and bubble release during alkaline water electrolysis by tailoring the architecture and surface properties of 3D-printed electrodes. The prepared electrodes consisted of 3D-printed nylon substrates coated with successive Cu and Ni layers via a deposition procedure. The electrodes were systematically characterized by different techniques combined with statistical methods to study (1) the resulting electrode quality, (2) effects of Ni deposition parameters on extrinsic properties and electrochemical performance, (3) the impact of the electrode architecture on bubble release, and (4) electrode performance and stability during water splitting. First, we confirmed the close relationship between the HER performance (using the chargetransfer resistance as a metric) and extrinsic properties by tuning the wettability, surface roughness, and the electrochemically active surface area (ECSA) of our 3D-printed electrodes. For this study, we fabricated four different electrode architectures consisting of cone, pyramid, rod, and oval patterns on the surface to examine the relationship between the electrode geometry and bubble release. We found that cone- and oval-patterned electrode architectures resulted in lower HER overpotentials (~40 mV decrease at 10 mA·cm⁻² between oval and planar geometries). We also found a comparable improvement for the

OER between the cone and planar geometries (~60 mV decrease at 10 mA·cm⁻²). These changes in HER and OER activity are attributed to differences in geometry and the shapes of each architecture. According to our results, larger bubbles emerging from macroscopic edges remain attached for longer times, increasing surface blockage and the ohmic resistance, which resulted in higher HER overpotentials for architectures with abundant edges (i.e., pyramid pattern). Furthermore, we found that this behavior occurs only on macroscopic features (>1 mm) by prototyping electrodes with micron-sized features via 3D printing. We also examined the performance and stability of 3D-printed porous electrodes with flow-through geometry, periodic structure, and large surface area. The 3D electrode resulted in enhanced bubble release compared to commercial nickel foam and exhibited a constant overpotential of ~300 mV (at 10 mA·cm⁻²) for the OER after prolonged activation, without noticeable signals coming from the Cu layer underneath. Finally, we demonstrate that these metal-coated 3Dprinted electrodes can act as suitable supports for electrocatalytic materials by depositing a benchmark NiFe electrocatalyst and testing its OER performance. The resulting NiFe/ 3D-Ni/Cu porous electrode exhibited a stable overpotential of ~250 mV (at 10 mA·cm⁻²) for over 20,000 cyclic voltammetry (CV) cycles with no structural or morphological changes. Thereby, ordered structures fabricated via 3D printing can act as promising supports for water electrolysis owing to their superior bubble release properties, electrochemical performance, and long-term stability.

2. RESULTS AND DISCUSSION

2.1. Fabrication and Characterization of 3D-Printed Electrodes with Planar Architecture. Unique electrode architectures were prepared via selective laser sintering (SLS) 3D printing. In SLS, a high-energy laser beam is focused over nylon 12 powder, fusing and linking the nylon 12 particles layer by layer according to a prescribed 3D model. The resulting plastic substrate is then coated with sequential metal layers, as depicted in Scheme 1. This multistep procedure is critical to (i)

Scheme 1. Fabrication of Ni, Cu-Coated 3D-Printed Nylon Electrodes through a Sequential SLS/Metal Deposition Approach



impart conductivity to the electrode and to (2) provide a HER/ OER active Ni coating through a simple and reproducible electrodeposition method. First, a thin Cu coating is deposited through an electroless plating technique, whereby Ag+ ions adsorbed on the nylon substrate's surface are reduced by formaldehyde into Ag nanoparticles. These nanoparticles act as catalytic seeds for Cu deposition by adsorbing formaldehyde and Cu ions, thereby decreasing the activation energy for the reduction of Cu by formaldehyde. 25,26 The electrically conductive, Cu-coated nylon substrates are then electroplated with a Ni layer, owing to its improved tolerance to alkaline media and the oxidizing conditions of the OER as opposed to Cu.²⁷, Ni electroplating was performed through a two-step electro-

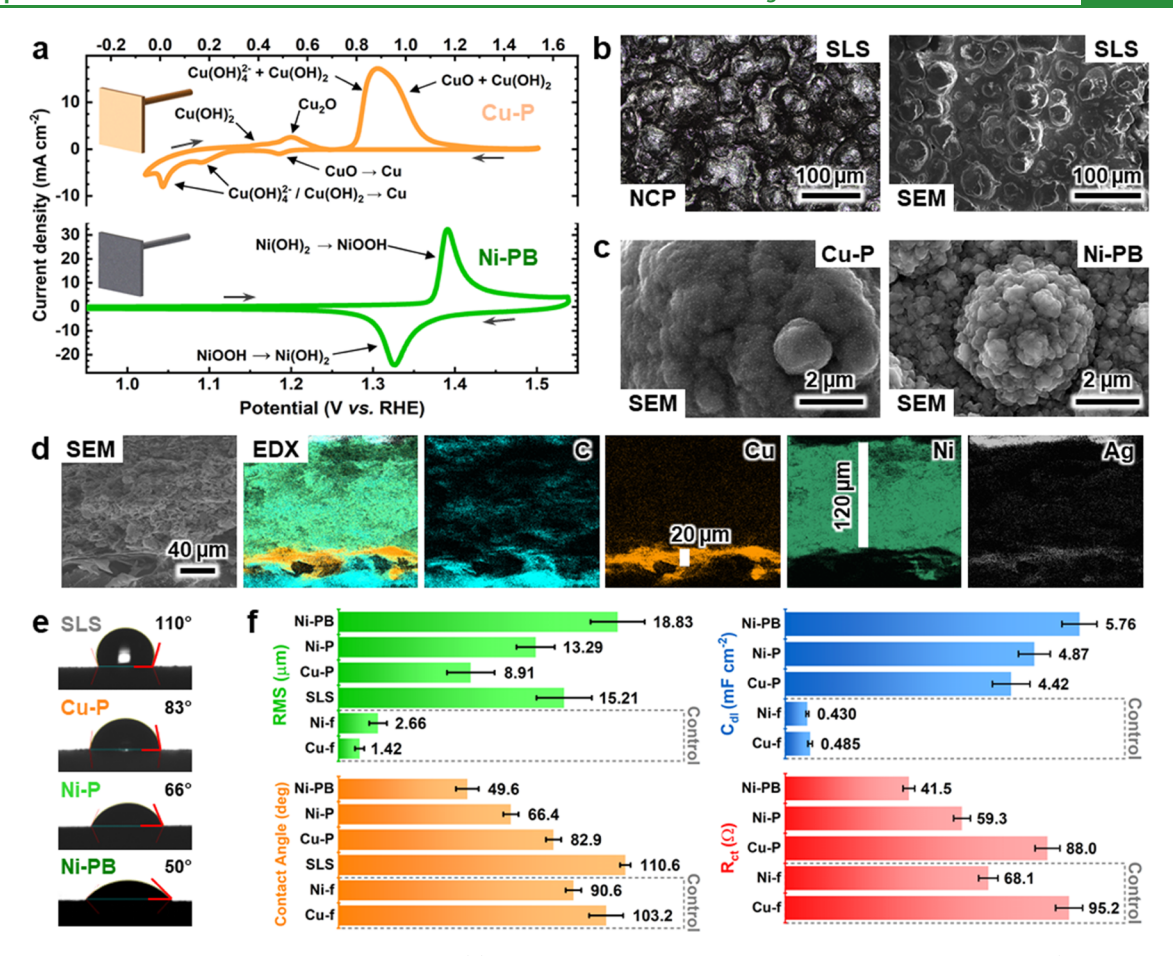


Figure 1. Characterization of planar 3D-printed electrodes: (a) CV scans of Cu-P and Ni-PB electrodes in Fe-free 1 M KOH (scan rate: $50 \text{ mV} \cdot \text{s}^{-1}$), (b) non-contact profilometry (NCP) and scanning electron microscopy (SEM) images of the 3D-printed planar nylon substrate, (c) SEM images of the deposited Cu and Ni films, (d) cross-sectional views and energy-dispersive X-ray (EDX) elemental mappings of the Ni-PB electrode, (e) contact angle of water droplets, and (f) quantitative evaluation of the root-mean-square (RMS) roughness, contact angle, C_{dl} , and R_{ct} of different planar electrodes. Control samples: Ni and Cu foils.

deposition process, whereby deposition of a relatively flat Ni coating (Ni-P, P: planar) is followed by deposition of Ni through hydrogen bubble template (HBT) electrodeposition. HBT is achieved by the simultaneous production of H₂ bubbles during Ni electrodeposition at high cathodic potentials, resulting in a dendritic porous structure with a large surface area and numerous Ni active sites.²⁹ The resulting electrode (denoted as Ni-PB, B: bubble) thus consists of a rigid nylon framework covered by a conductive Cu layer and an outermost rough Ni layer (exposed to the alkaline electrolyte) that provides Ni active sites for the HER/OER. A complete description of electrode dimensions and properties is shown in Table S1 in the Supporting Information. Hereafter, current densities normalized by the geometric surface area refer to the exposed area in Table S1, which is the total exposed surface area calculated from 3D models. This 3D printing-metal deposition methodology provides a convenient approach to obtain conductive electrodes with specific architectures for fast prototyping enabled by SLS 3D printing.

As depicted in Scheme S1, we tested how surface properties and architectures of our 3D-printed electrodes affected the electrochemical performance, stability, and bubble release during water electrolysis. Five main avenues are explored in this study: (i) the quality of deposited metal coatings, (ii) the effects of the HBT electrodeposition conditions on extrinsic electrode properties and their relationship with HER perform-

ance, (iii) the impact of electrode architecture on bubble removal during water splitting, (iv) the electrochemical performance and stability of a 3D porous electrode with periodic architecture, and (v) the performance of the 3D-printed porous electrode acting as a support for a benchmark NiFe electrocatalyst. Through these five approaches, we demonstrate how tailored 3D-printed electrodes can be optimized to control extrinsic electrode properties and improve bubble release, enabling a controlled and reproducible way to examine electrocatalytic materials and enhance electrochemical performance.

First, we characterized the morphology, elemental composition, and surface properties of 3D-printed planar electrodes (Figure 1). Cyclic voltammetry (CV) scans were recorded to reveal the redox properties of the electrodes (Figure 1a). After Cu deposition, the Cu-P electrode (P: planar) exhibited a typical voltammogram of bulk copper, 30 with redox peaks ascribable to surface Cu oxidation and reduction. Adequate coverage of the substrate by Ni was confirmed by the lack of redox peaks corresponding to Cu in the Ni-PB sample. Instead, only Ni $^{2+/3+}$ redox peaks were detected (Figure 1a) around 1.37 V vs reversible hydrogen electrode (RHE), as previously reported. 28,31 Additionally, X-ray diffraction (XRD) patterns for each layer were recorded (Figure S1). As depicted in Figure S1a, the XRD pattern of the SLS substrate after sintering exhibits a strong diffraction (2θ : 20.1°) corresponding to the (001) plane

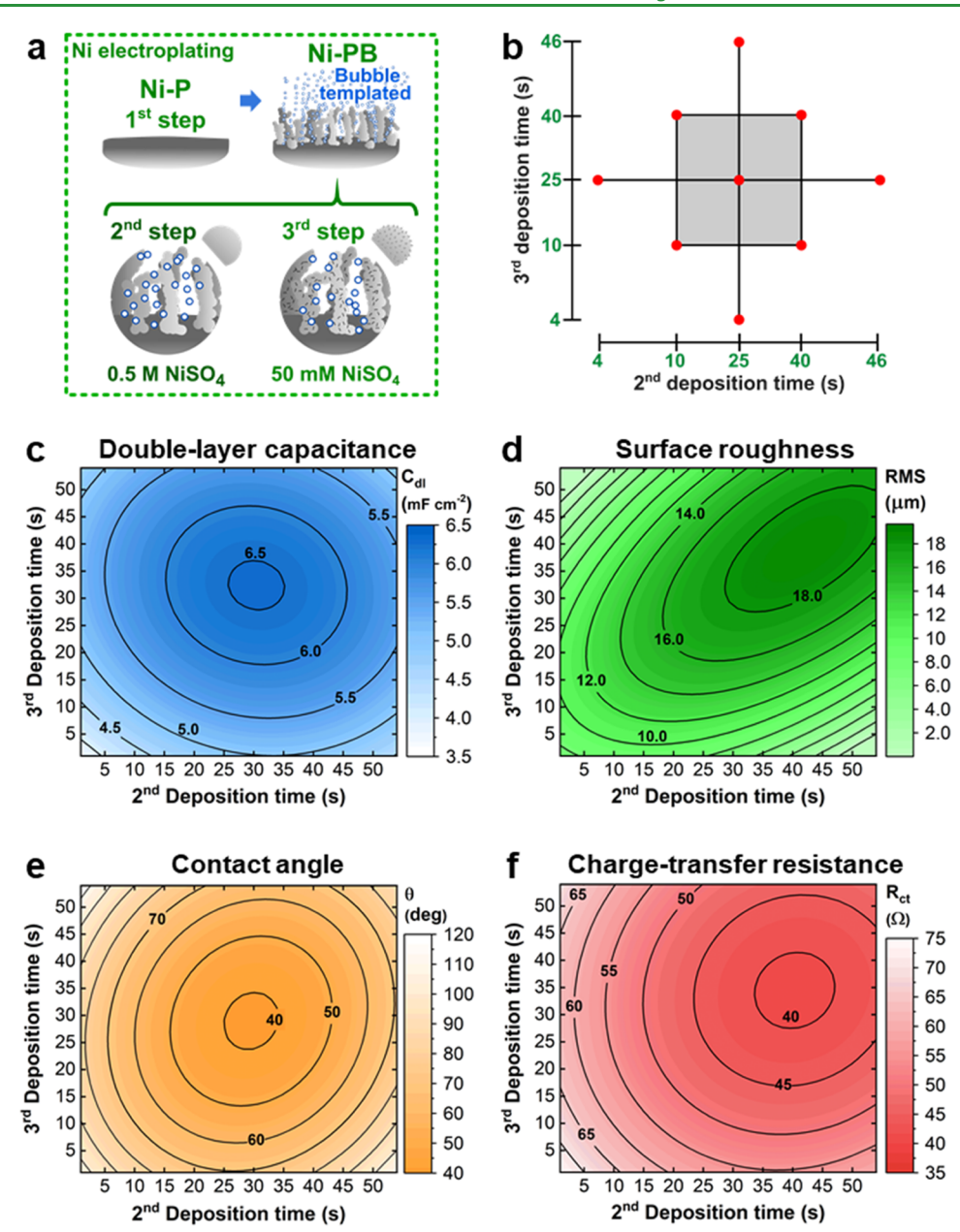


Figure 2. Evaluation of deposition times on the HBT electroplating step: (a) schematic illustration of the sequential HBT steps, (b) deposition times for the RSM design, 3D surface mappings for the studied responses, (c) C_{dl} (d) RMS roughness, (e) contact angle, and (f) R_{ct} .

of the stable γ -phase crystal of nylon 12. ³² XRD patterns of successive metal coatings show the typical peaks for (111), (200), and (220) facets of cubic Cu and Ni crystals. ^{21,24} Additional grazing incidence X-ray diffraction (GIXRD) measurements of the metal coatings (Figure S1b) confirmed that no Cu was exposed following the Ni deposition synthetic step, as there was effectively no signal from Cu or the underlying nylon 12 substrate. XPS analysis of the Cu/SLS and Ni/Cu/SLS electrodes revealed the presence of Cu(0) and Ni(0) states (Figures S2), thereby confirming the metallic character of both films. Cu LMM Auger analysis of the Cu/SLS electrode confirmed the existence of Cu(0), Cu₂O, and Cu(OH)₂ species (Figure S2b). Figure S2d confirms the absence of Cu at the top of the Ni/Cu/SLS electrode.

We characterized surface topography and morphology using non-contact profilometry (NCP) and scanning electron microscopy (SEM). NCP images of the nylon substrate show

numerous protrusions emerging from the surface (Figures 1b and S3), attributed to the sintering of nylon particles. The same morphology is observed from SEM images after coating the nylon substrates with a conductive Pd/Au layer. Deposition of Cu and Ni layers increased the surface roughness (Figure 1c). In particular, the Ni-PB sample after HBT electrodeposition showed numerous spikes protruding from Ni structures (see also Figure S4), attributed to the use of plating baths with different Ni concentrations (see the Section 4). Cross-sectional images were taken from Ni-PB electrodes to visualize the layered structure of the metal coatings. SEM images and elemental mappings via energy-dispersive X-ray (EDX) spectroscopy revealed distinct Cu and Ni layers, as shown in Figure 1d. Additional cross-sectional EDX mappings reveal a consistent Ni layer that prevails among replicates (Figure S5). Whereas the Cu layer (thickness: $30 \pm 5 \mu m$) penetrates the holes and pores of the rough nylon substrate, the Ni layer exhibits a continuous,

packed layer with a thickness of 135 \pm 15 μ m. Ag catalytic seeds can also be seen in the same area covered by the Cu coating, confirming the effectiveness of the method proposed by Wang et al. for electroless Cu deposition. 25 Note that the presence of Ag on top of the Ni layer is caused by the silver conductive epoxy coating used for making cross-sectional cuts (see the Section 4). The Cu coating was preserved after adhesion tests based on the ASTM D 3359 standard (i.e., tape test), as shown in Figure S6, confirming that the adhesion of the Cu layer was strongly secured to planar nylon substrates (Figure S6c). Electroless deposition times over 60 min resulted in Cu films that peeled off easily (Figure S6d) compared to the optimal conditions given by Wang et al. (i.e., 40 min), demonstrating the importance of deposition time to provide strong adhesion.²⁵ We attribute superior adhesion to strong chemical bonding of thiosulfate—Ag complexes with the rough nylon substrate, which provided numerous anchors for the Cu metal coating.

We assessed three key surface properties to quantitively examine the extrinsic factors of our 3D-printed planar electrodes. (1) We measured the contact angle (θ) between a water droplet and the electrode surface as a measure of surface wettability; (2) surface roughness was determined by calculating the root-mean-square (RMS) roughness from NCP imagery representative of the 3D surface; and (3) the double-layer capacitance (C_{dl}) determined from CV scans in the non-faradaic region at different scan rates (see Figures S7 and S8a) was used as a proxy for the electrochemically active surface area (ECSA). Furthermore, we evaluated the electron-transfer resistance during the HER by measuring the charge-transfer resistance (R_{ct}) through electrochemical impedance spectroscopy (EIS). We utilized the R_{ct} as a measure of HER capability to examine its relationship with the three extrinsic properties listed above. Successive metallic layers increased the surface wettability, as shown by decreased contact angle (Figure 1e). Notably, contact angles of the best-performing electrode (Ni-PB) were smaller than those reported for NiFe-layered double hydroxide (LDH) pyramid electrodes (i.e., 62°), which is attributed to the increased roughness produced during HBT electrodeposition of the Ni-PB electrode, as high roughness is critical for increasing hydrophilicity. Similar trends were found for the rest of the surface properties, as displayed in Figure 1f. RMS roughness increased with successive coatings, which agrees with the increase in the $C_{\rm dl}$ (i.e., ECSA). Using a standard specific capacitance (C_s) of 40 μ F·cm⁻² for Ni(OH)₂, ³³⁻³⁵ the Ni-PB sample exhibited an ECSA of 144.8 cm², corresponding to a roughness factor (RF) of 17.6 (based on the exposed area calculated from the 3D models using SolidWorks, Table S1). The R_{ct} decreased with increasing roughness, suggesting faster electron transfer and better HER performance due to the increased ECSA (see also Figure S8b for corresponding Nyquist plots). Our metal-coated electrodes exhibited superior properties compared to commercial metallic foils (Cu-f, Ni-f) used as control samples (Figure 1f). Furthermore, low relative standard deviations (RSD < 10%) from the error bars of our replicates in Figure 1f confirm the reproducibility of our deposition methodology. Hence, the Ni-PB electrode had the largest surface area due to the increased roughness, the fastest electron transfer, and the most hydrophilic surface, thereby increasing contact with the electrolyte and providing more active sites for water splitting. 21,36,37

2.2. Effects of Ni Electroplating Conditions on Extrinsic Electrode Properties. Extrinsic properties (RMS roughness, contact angle, and $C_{\rm dl}$) of the 3D-printed Ni-PB

planar electrodes were characterized as a function of HBT electroplating deposition time. We also measured the R_{ct} to examine the relationship between these properties with HER performance. Our Ni electrodeposition methodology involves three electrodeposition steps (Figure 2a): (1) deposition of the uniform Ni-P coating to prevent the inner Cu layer from being exposed to the electrolyte, (2) deposition of a rough Ni layer using a concentrated Ni bath to deposit numerous protrusions, and (3) deposition of a refined Ni layer using a diluted Ni salt aqueous solution to increase the surface roughness. Only steps 2-3 follow the HBT electrodeposition technique; thereby only the deposition times of these were systematically varied. Experiments were performed using a response surface method (RSM) statistical design (Figure 2b) to document the relationship between deposition times and each property of interest (i.e., RMS, θ , C_{dl} , R_{ct}). Each response (z axis) is measured individually at a given set of deposition times (x, y axes)for second and third Ni deposition steps, respectively). Then, the properties are mapped out over the entire x,y space, creating a heat map from quadratic models that can also be used to predict the response.

3D surface mappings for each extrinsic property are depicted in Figure 2c-f. Second-degree models (i.e., quadratic equations) and additional statistical results are summarized in Table S2. All models showed large correlation coefficients (adj. $R^2 > 90\%$), suggesting a strong correlation between the deposition times and the studied properties. For the ECSA, Figure 2c shows a maximum $C_{\rm dl}$ around deposition times of 30 s for both steps (corresponding ECSA: 157.9 cm², RF: 19.1). Similarly, the R_{ct} is minimized at approximately x = 35, y = 35 in Figure 2d. As depicted in Figure 2e, RMS roughness increased at higher deposition times for both steps. Finally, the contact angle was minimized at the center of the map (Figure 2f). These results suggest that these extrinsic properties can be precisely tailored just by controlling the Ni deposition times. As increasing the time of only one HBT electrodeposition step did not significantly improve the resulting electrodes, both abundant protrusions (i.e., second step) and augmented surface roughness (i.e., third step) are required to yield the best-performing Ni-PB electrode. Furthermore, these three properties are closely related to HER capability as the R_{ct} exhibited a similar optimal spot around the (35, 35) coordinate, suggesting that tuning these extrinsic properties also results in different HER performance. These results suggest that even slight differences in surface roughness, wettability, and the ECSA can induce changes in the electron-transfer capability, resulting in different electrochemical performances. Hence, researchers should consider the effect of these extrinsic properties to provide accurate and comparable measurements. These findings demonstrate that hydrophilic surfaces with large surface area and fast electron transfer can be effectively constructed by tunable electrodeposition steps, allowing for controllable and reproducible production of 3Dprinted electrodes for water electrolysis.

2.3. Electrode Architecture Effects on Bubble Release during the HER. The electrode geometry is another extrinsic property that has been shown to influence the performance of water electrolysis. ^{6,7,21} We assessed the relationship between the electrode geometry and bubble release as a function of four macroscopic geometric patterns: cones, pyramids, cylindric rods, and elliptic (oval) cylinders (Figure 3a). Detailed properties of these patterns are shown in Table S1. These patterns, adopted following recent electrode studies, ^{19,21,22,38} approximately double the exposed geometric area compared to

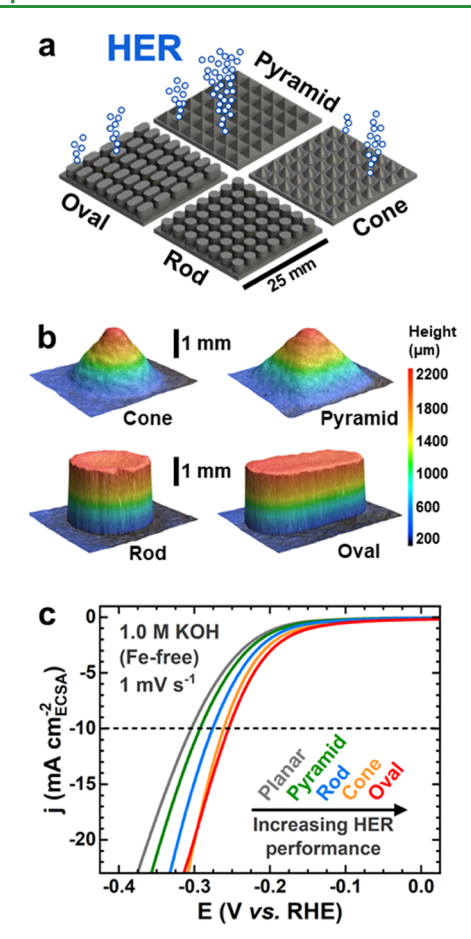


Figure 3. Electrode architecture effects on bubble release during the HER: (a) scheme of the examined electrode geometries, (b) NCP 3D mappings of the surface shapes, and (c) LSV scans in HER region for each electrode architecture.

planar electrodes, thereby increasing contact between the Ni active sites and the electrolyte. ²¹ The surface roughness of these patterns was measured by NCP from 3D surface images (Figure 3b, see also Figure S9). Linear sweep voltammetry (LSV) curves were recorded in the alkaline electrolyte to evaluate the impacts of the geometry on HER activity. As shown in Figure 3c, the overpotential necessary to achieve a current density of -10 mA· cm⁻² varies by the electrode architecture even when the current density is normalized by the ECSA. Notably, the oval electrode requires the lowest overpotential (235 mV) among all of the samples to obtain $-10 \text{ mA} \cdot \text{cm}^{-2}$, improving HER activity by 40 mV compared to the planar electrode (275 mV). Additional HER chronopotentiometric tests at −10 mA·cm⁻² during 20 h (Figure S10) further confirm the changes in the overpotential for each architecture. Notably, the oval and cone architectures exhibit the lowest overpotentials, improving the HER by ~50 mV compared to the planar electrode.

To further assess the origin of this activity enhancement, bubble evolution tests at a constant current density of $-10 \, \text{mA} \cdot \text{cm}^{-2}$ were recorded with an optical microscope to monitor bubble population and detachment for each electrode architecture. For these tests, the electrodes were placed inside a custom electrochemical cell equipped with a quartz window (see Figure S11) at 20 °C. The cell and optical microscope were positioned at an angle of 45° to avoid bubble agglomeration over the quartz window. The KOH electrolyte was degassed with ultrahigh purity Ar for 30 min to remove

dissolved gases before bubble evolution tests. Maximum diameters of several bubbles (n = 50) upon departure from the electrode surface were measured from digital recordings taken with an optical microscope (Video V1) at 20.1 °C. Histograms showing the maximum bubble diameter at departure are shown in Figure S12. According to analysis of variance (ANOVA) tests, only the cone geometry had statistically significant ($\alpha = 0.05$) smaller bubble diameters compared to the rest of the geometries when measured randomly across the entire electrode surface, suggesting that bubble removal was not significantly different among the studied architectures. However, the diameters of bubbles detaching from geometric edges and planes for each electrode architecture differed (Figure 4a). Note that we consider sharp turns in the geometry as "edges" while "planes" refer to flat and curved surfaces without abrupt slope changes (Scheme S2). Furthermore, we use these terms only for geometric features at the macroscopic scale and not for structural defects or edges in the crystalline structure.

We carefully examined the properties of bubbles departing from edges and planes. In terms of size uniformity (i.e., bubble size similarity between edges and planes), the bubble diameters of the edges and planes of cone and oval geometries were statistically comparable (according to ANOVA tests), meaning that there was no significant change in size compared to those emanating from the edges and planes of pyramid and rod architectures (i.e., nonuniform size distribution). For pyramid and rod patterns, edge-departing bubbles had significantly larger diameters than plane-departing bubbles, suggesting that geometric edges could be the limiting factor in terms of bubble size. These observations indicate that these geometries induce different bubble diameters, changing the bubble size distribution across the electrode surface. To further examine the effects from geometric edges and planes in our architectures, we monitored bubble lifetime (*i.e.*, the period from noticeable nucleation until detachment) for each geometric pattern (Figure S13). As depicted in Figure 4b, bubble lifetimes between edges and planes were also the shortest and most similar for cone and oval patterns. Furthermore, bubble lifetimes on planes are comparable for all architectures, suggesting that the bubble evolution on edges limits the performance. Thus, in terms of lifetime uniformity, only the cone and oval architectures exhibit similar bubble evolution across the electrode surface. These results suggest that a relationship between electrode architecture and bubble release exists. These trends also match with HER activity differences in Figure 3, suggesting that the electrode architecture impacts HER performance via changes in the bubble release behavior depending on certain geometric features, the cone and oval resulting in uniform bubble sizes across the electrode surface.

We speculate that the observed bubble release trends are linked to specific geometric properties that impact the bubble triple-phase contact line, including (1) relative abundance of geometric edges and planes, (2) inclined planes that create asymmetrical bubble shapes with varying contact angles, thereby modifying the buoyant and adhesion forces around the bubble, (3) boosted coalescence of neighboring bubbles at preferred angles and geometries, and (4) a discontinuous triple interface (electrode/bubble/electrolyte) that reduces the true contact area and adhesion forces depending on the location (*i.e.*, edges and planes).^{8,9,39} Regarding our electrode architectures, the following aspects can be summarized. First, bubble release effects could be related to the differences in the abundance of

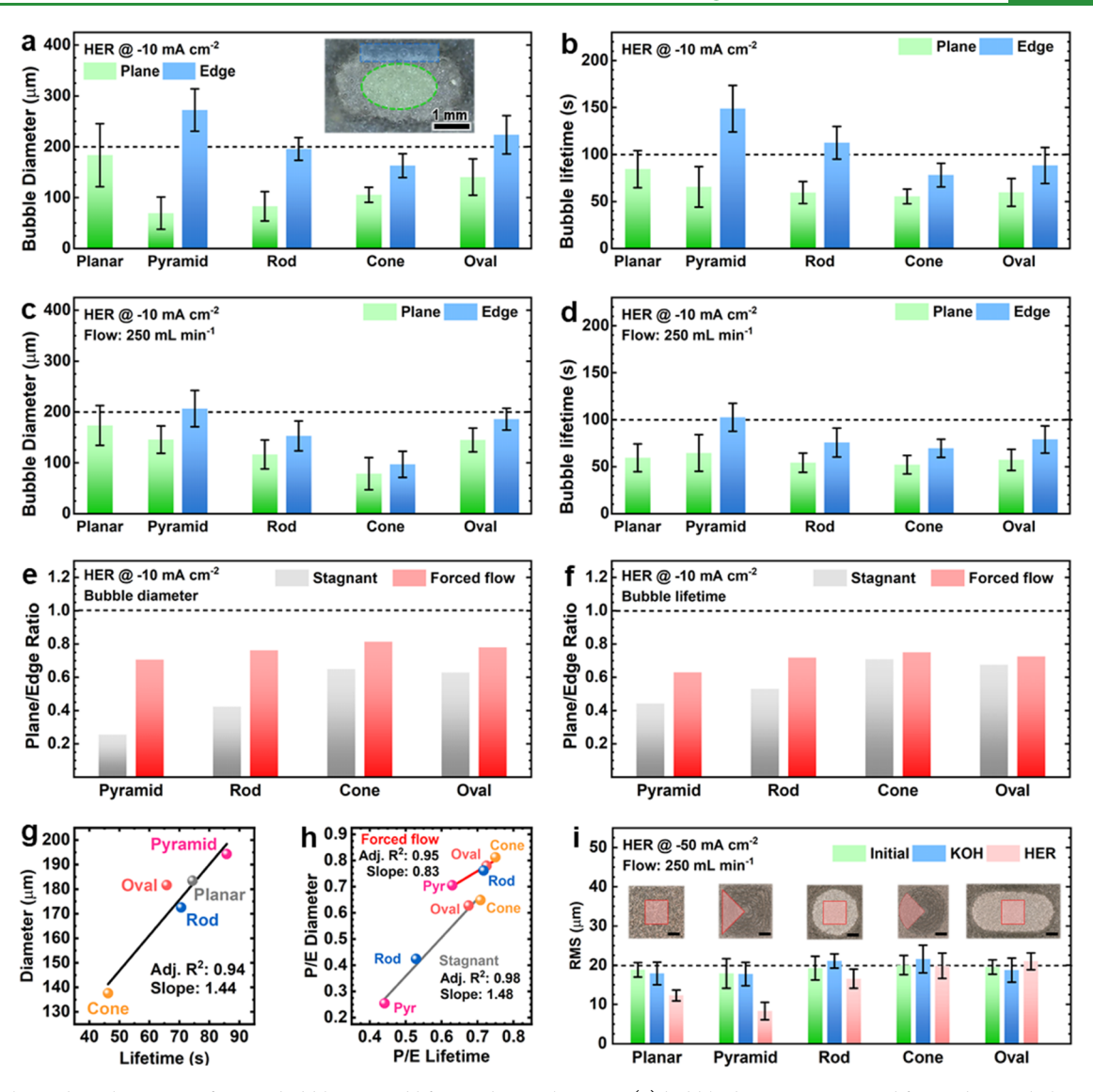


Figure 4. Electrode architecture effects on bubble size and lifetime during the HER: (a) bubble diameters measured from edges and planes (inset: an image of the oval electrode during HER evolution tests), (b) bubble lifetimes from edges and planes, (c) bubble diameters and (d) lifetimes from edges and planes under forced flow conditions (250 mL·min⁻¹), plane/edge ratios for (e) bubble diameters, (f) lifetimes under stagnant and forced flow conditions for the studied electrode architectures, (g) plot of bubble diameter ν s bubble lifetime for different geometries under stagnant conditions, (h) plot of the planar/edge ratios under stagnant and forced flow conditions, and (i) electrode roughness before and after KOH electrolyte immersion and prolonged HER tests at -50 mA cm⁻² (insets: examined surfaces for each electrode; scale bar: 500μ m). Dashed lines are used for reference only.

edge and plane features. The pyramid architecture contains several edges, while the cone geometry contains a continuous, curved surface without noticeable edges other than the tip and the base of the cone (Scheme S2). Therefore, abundant geometric edges in the pyramid architecture may induce larger bubbles that reside for longer periods, resulting in increased surface coverage, higher ohmic resistance, and, therefore, larger overpotentials.⁸ Regarding oval and rod architectures, although both have the same projected area of the planar electrode (i.e., 6.25 cm²), the rod architecture is covered by 49 cylinders, while the oval architecture contains 40 elliptic cylinders with a larger plane area on the top. Considering the entire electrode, the rod architecture exhibits more edges and corners than the oval electrode. Nevertheless, their bubble size and lifetime distributions are quite similar (Figure 4a,b) compared to the noticeable difference between cone and pyramid architectures. Second, inclined planes may also play an important role. For instance, pyramid and cone architectures exhibited the smallest

bubbles (<100 μ m) detaching from planes, and only those emerging from edges caused disparities in size for the pyramid architecture (Figure 4a). Third, improved bubble release on planes can be explained by the coalescence of neighboring bubbles. In fact, the top planes of oval and rod shapes are not completely flat, and they appear to be slightly concave (see Figure S9). Thus, bubbles could have been forced inward (i.e., toward the center of these planes), increasing the population of bubbles and favoring coalescence. Finally, increased surface roughness combined with macroscopic curvature (e.g., from conical shapes and concave top planes of cylinders) may decrease the true contact area between the bubble and the surface, owing to a discontinuous surface filled with gas pockets, thereby decreasing the adhesion force.^{8,11} Considering these geometric properties favor bubble detachment on planes, trends observed in Figure 4a,b suggest that bubble release on geometric edges is the main limiting factor.

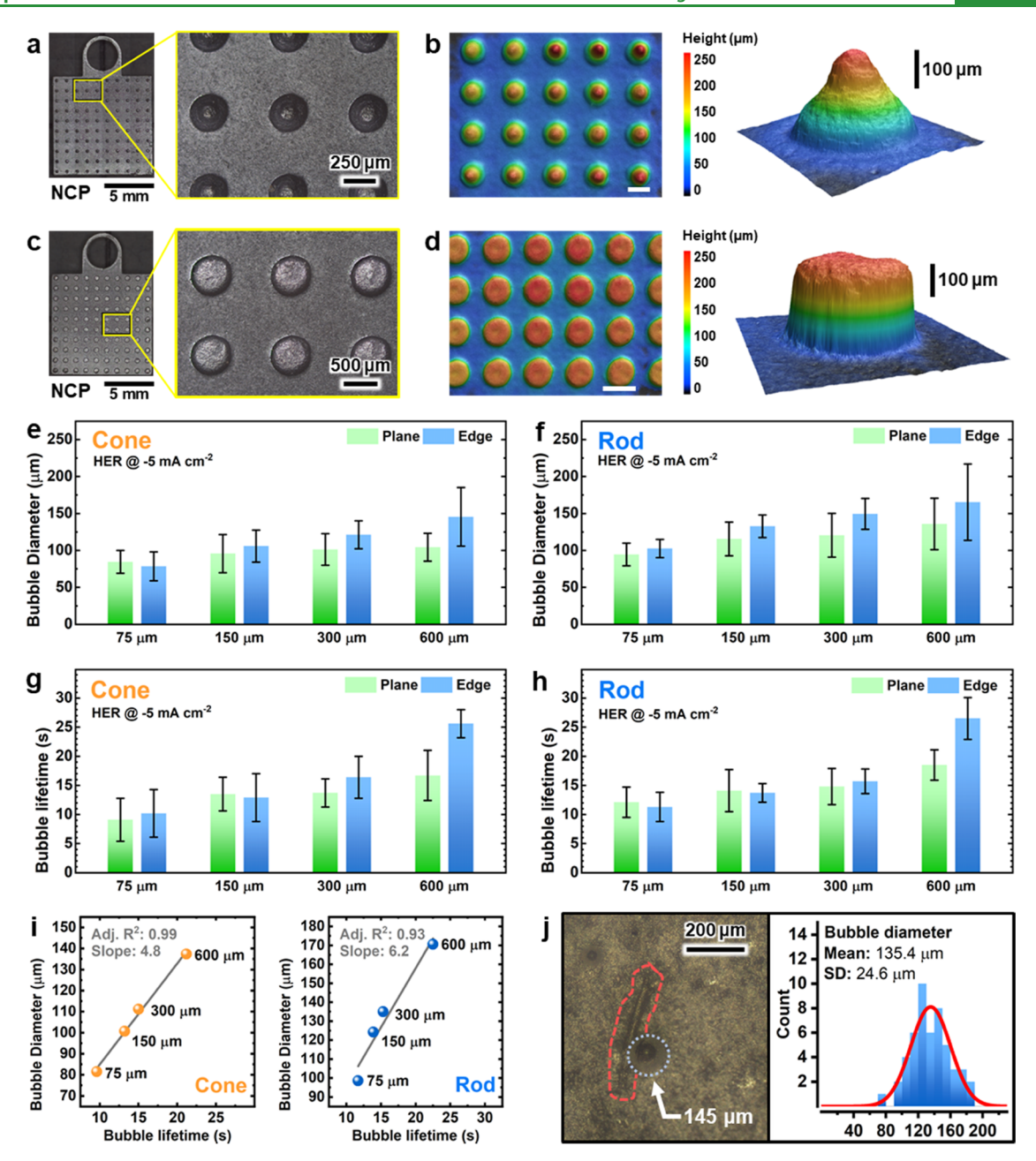


Figure 5. Electrode feature size effects on bubble size and lifetime during the HER: (a) NCP images and (b) 3D mappings of the electrode with conelike features (diameter from scale bar: $300 \, \mu \text{m}$), (c) NCP images and (d) 3D mappings of the electrode with rod-like features (diameter from scale bar: $600 \, \mu \text{m}$), bubble diameters measured from edges and planes in (e) cone and (f) rod features, bubble lifetimes measured from edges and planes in (g) cone and (h) rod features, (i) plots of bubble diameter vs bubble lifetime for the cone and rod geometries under stagnant conditions, and (j) NCP image and bubble diameter distribution of a crevice located on a flat surface in between cones of the cone electrode.

Local changes in wettability due to nonuniform surface roughness and hydrophobic heterogeneities may also induce different bubble dynamics at edges and planes, as suggested previously. More studies of geometric surface effects are needed to decipher controls of bubble sizes and lifetimes. Particular attention should be paid to bubble evolution on well-controlled geometric features (such as planes with different tilting angles or different edge/plane ratios). Even bubble release at the nanoscale needs to be examined to reveal interfacial dynamics and the relationship between triple-phase contact lines and bubble diameters at departure. These studies are beyond the scope of this study, and further research should focus on these aspects to provide a clear understanding of the role of

macroscopic effects on bubble release and HER performance. Nevertheless, our results confirm that subtle HER activity changes arise from changes in the electrode architectures, thereby influencing the bubble release and improving HER activity as small bubbles (with more uniform size distributions over the electrode) are produced.

Moving forward, we also examined the role of controlled electrolyte convection in improving the bubble release of the electrode architectures. Circulating the electrolyte during water electrolysis has proven beneficial as it refreshes the electrode surface, reduces interfacial supersaturation of dissolved gases, and improves the mass transfer of reactants and products. 8,23 Although most industrial electrochemical processes operate

under controlled electrolyte flow conditions, 41 few studies have analyzed the effect of forced electrolyte convection on electrochemical systems with ordered electrode architectures. Accordingly, bubble evolution tests were repeated using the same custom electrochemical cell (Figure S11) but with the KOH electrolyte pumped parallel to the electrode surface at a constant flow rate of 250 mL·min⁻¹, based on our previous study.²³ Recordings are available in Video V2. As shown in Figure 4c,d, flowing the electrolyte decreased the bubble sizes and lifetimes in all of the studied architectures compared to nonflow conditions (Figure 4a,b, see also Figures S12-S14). Continuous electrolyte flow also resulted in more uniform size and lifetime distributions, with no significant statistical difference between bubbles evolved at edges or planes (Figure 4c,d). We use a dimensionless plane-to-edge ratio (P/E) to quantitatively estimate the similarity between bubble sizes and lifetimes at edges and planes. This parameter represents the bubble lifetime (or diameter) ratio at a plane and an edge. Hence, a P/E = 1 means that bubble lifetimes (or diameters) are equal at planes and edges. For the stagnant and controlled flow tests, Figure 4e shows P/E ratios for bubble diameters at departure, while Figure 4f shows P/E ratios for bubble lifetimes. In all the cases, P/E ratios are below 1, suggesting that bubbles evolved from geometric planes are smaller and have shorter lifetimes than those emanating from the edges. However, flowing the electrolyte increased the P/E ratio above 0.6, with all electrode architectures exhibiting P/E ratios between 0.6 and 0.8. These results suggest that controlled electrolyte flow systematically decreases bubble sizes and lifetimes on edges, regardless of the electrode architecture, thereby resulting in more uniform size and lifetime distributions. Forced electrolyte convection also resulted in comparable HER performance, as confirmed by LSV curves under electrolyte flow (Figure S15). Nevertheless, forced convection demands extra energy necessary for pumping the electrolyte, and therefore it must be carefully optimized depending on the electrolyzer design and pressure drop, as we demonstrated in a previous study.²

We compared the performance between stagnant and controlled flow electrolyte conditions for all of the studied architectures by normalizing bubble sizes and lifetimes. The relationship between average bubble size and lifetime for each electrode architecture is linear under stagnant conditions, with the cone pattern exhibiting the smallest diameter and shortest lifetime (Figure 4g). Similar trends can be seen when the P/E ratios are plotted instead (Figure 4h). The good linearity for both stagnant and flow conditions (adj. $R^2 > 0.95$) confirms the proportionality between bubble size and lifetime. The forced flow condition results in higher P/E ratios (i.e., decreased bubble sizes and lifetimes on edges) for bubble sizes and lifetimes, as previously discussed. The slope for stagnant conditions (1.48) is nearly twice that for controlled electrolyte flow (0.83), and the linear range of the controlled flow condition is restricted to a narrower lifetime range (0.6-0.8), suggesting that the electrode architectures (particularly oval, cone, and rod shapes) have comparable P/E ratios, and therefore, similar bubble release. These trends demonstrate that flowing the electrolyte improves bubble release on edges and results in comparable properties for the electrode architectures. Hence, pumping the electrolyte results in a more homogeneous bubble release, almost invariant of the electrode architecture.

Intrigued by the potential role of bubbles in modifying the surface of our electrodes, we assessed the surface roughness consistency (via NCP) before and after vigorous HER. Because

electrode roughness was unaltered after 24 h exposure to KOH electrolyte under controlled pumping, changes in the RMS roughness should be ascribable only to HER. We found that all electrode geometries, except planar and pyramidal, conserved their roughness after HER tests at -50 mA·cm⁻² for 24 h (Figure 4i). We suspect that the significant decrease in RMS roughness for the pyramid architecture originates from larger bubbles detaching from edges that ablate the surface through structural oscillations and cavitation. 8,42,43 Given the same spot was analyzed for bubble diameter and lifetime before and after KOH immersion and HER testing, these results are validated despite a lack of overall change in the bulk structure, as indicated by a nearly unchanging ECSA for each electrode geometry (Figure S16). Hence, local roughness measurements are thus needed to reveal surface damage due to bubble evolution. Although beyond the scope of this study, further studies of electrode architectures and associated surface changes during bubble evolution should improve electrode designs for largescale water electrolysis.

Owing to the increasing capabilities of 3D printing to construct precise microstructures, ²¹ we also examined the role of the structure size on bubble size and lifetime during the HER. Cone and rod-like features ranging from 75 to 600 μ m in diameter and a constant height of 250 μm were fabricated through stereolithography (SLA) 3D printing due to its improved printing resolution compared to SLS. As depicted in Figure 5a-d, the electrodes comprised arrays of these features on a planar surface of 1 cm². Maximum bubble diameters and bubble lifetimes upon detachment from the surface were measured from recordings, and photos were taken with an optical profilometer (Figure S17). These measurements were made possible by placing the electrodes into a custom visualization cell made of poly(tetrafluoroethylene) (PTFE) and applying a constant current of $-5 \text{ mA} \cdot \text{cm}^{-2}$. As shown in Figure 5e,f, the maximum bubble diameter decreases as the size of the cone and rod structures decreases. Typical snapshots taken during bubble evolution depict bubbles emerging from edges and planes on the cone and rod features (Figure S17b,c). The same trend can be observed for bubble lifetimes (Figure 5g,h). Moreover, a linear relationship between bubble diameter and lifetime can be seen in Figure 5i for both geometries. However, there is no statistical difference among these structure sizes in Figure 5e-h since the standard deviations (from bubble diameter and lifetime histograms, n = 50) overlap, most notably for structure sizes below 300 μ m. There is also no significant difference between bubbles emerging from planes vs edges, suggesting that bubble evolution at micron-sized structures $(75-600 \mu m \text{ in diameter})$ does not change based on the location, as it occurred with macrostructures (~3 mm in diameter, results shown in Figure 4).

Interestingly, bubbles emerging from a crevice located on the space in between the cones (Figure 5j) exhibited bubble diameters around 135 μ m, and the bubble diameter distribution statistically overlaps with the diameters of bubbles emerging from 150 to 600 μ m wide cones (Figure 5e). This crevice was not intentionally placed on the electrode and resulted from its proximity to the electrode's corner and scratching caused during handling of the material. These results suggest that discrepancies between bubbles emerging from the plane and edge sites do not prevail on microstructures, contrary to macrostructures with features above \sim 1 mm (Figure 4). This phenomenon could be explained by the similar size between the various geometry types that rises with decreasing feature size (going from macro to

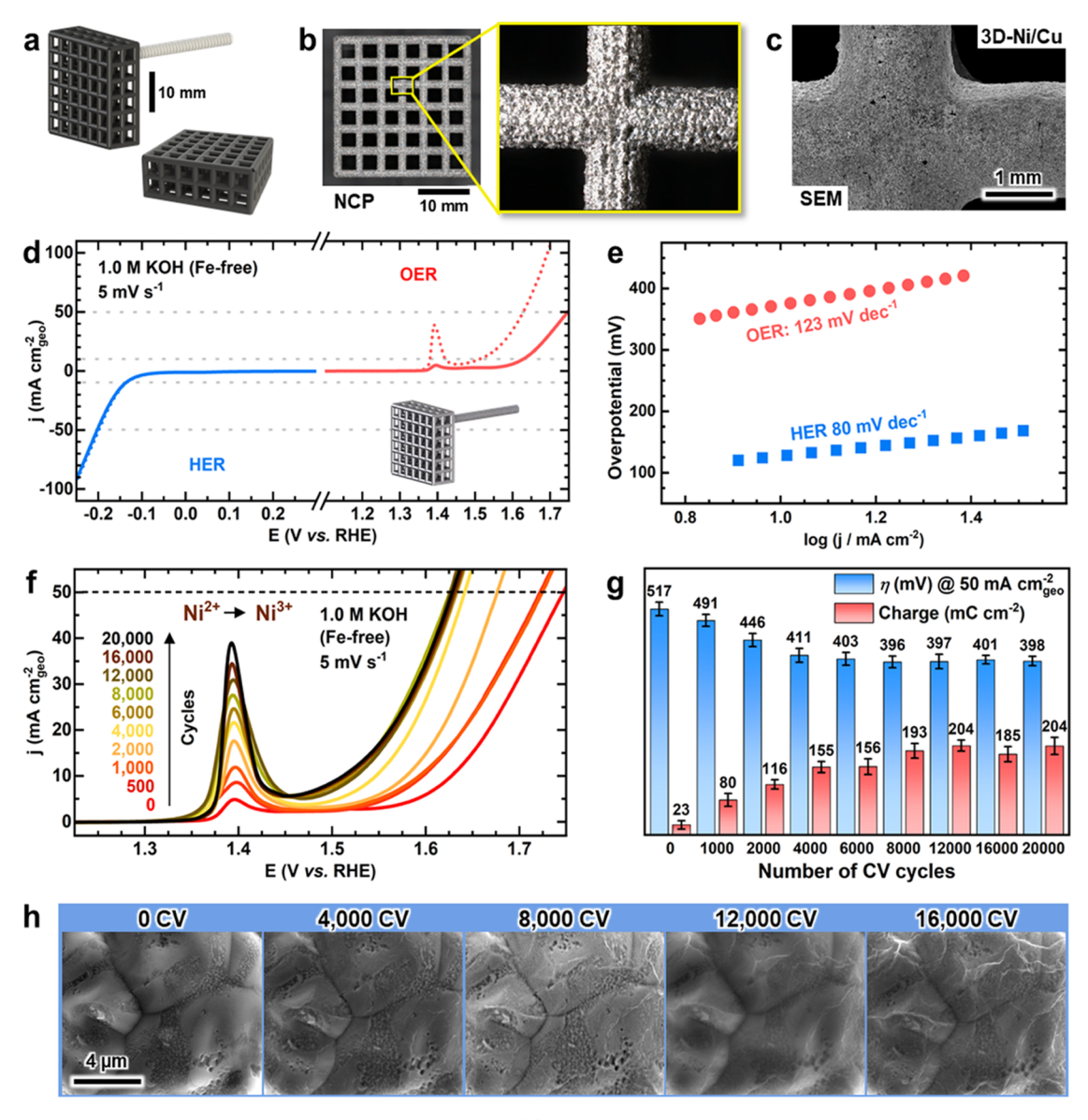


Figure 6. Characterization and evaluation of the 3D porous electrode: (a) schematic illustration of the 3D-printed nylon porous electrode, (b) NCP and (c) SEM images of the Ni-coated 3D porous electrode, (d) HER and OER polarization curves of the 3D-Ni/Cu porous electrode before (solid line) and after (dashed line) stability tests (HER: CP at 10 mA·cm⁻², OER: 20,000 CV), (e) Tafel slopes, (f) evolution of the Ni^{2+/3+} redox peak during OER cycling of the 3D-Ni/Cu porous electrode, (g) overpotential @ 50 mA·cm⁻² and charge of the Ni^{2+/3+} redox peak variation during OER cycling, and (h) identical-location SEM images of the 3D-Ni/Cu porous electrode during OER cycling.

micro), as the comparable sizing between the different geometries would result in gas pockets of similar dimensions, yielding bubbles of similar size and lifetime. This explains why the crevice shown in Figure 5j exhibited a comparable bubble diameter distribution, as the gas pockets around scratches or crevices could be virtually the same as those around cone and rod shapes, resulting in comparable H₂ bubble formation. 8 As a result, we theorize that the plane vs edge bubble evolution distinction only applies to macrostructures where gas pockets and surface defects vary depending on the geometry features. Also, bubble sizes become greater than the characteristic dimensions of the cone and rod shapes as their sizes decrease (e.g., shapes 75 μ m wide), resulting in bubbles that occupy large portions of the microstructure, making it difficult to distinguish gas evolution from different spots. Since the study of nanobubble formation is beyond the scope of this study (due to evident limitations of our 3D printing capabilities), we

encourage further study of smaller bubbles to elucidate if these trends prevail on even smaller features and/or different geometries.

Finally, we also examined the properties of bubbles departing from edges and planes during oxygen evolution. LSV scans recorded in the OER region (Figure S18a) resulted in different OER overpotentials depending on the electrode architecture, with the cone architecture exhibiting the lowest overpotential (\sim 530 mV@10 mA·cm⁻²) and surpassing the planar electrode by \sim 60 mV. Bubble diameters (Figure S18b) and lifetimes (Figure S18c) of edges and planes were not statistically different from one another, with the exception of the pyramid architecture. As depicted in Figure S18d, O₂ bubble diameters and lifetimes among the studied architectures follow a linear relationship, where cone architecture results in the shortest lifetimes and diameters. Furthermore, average O₂ bubble diameters were larger and lifetimes longer than those of H₂

bubbles (Figure 4a,b) for all of the studied architectures. This behavior can be explained by the distinct coalescence characteristics of H₂ and O₂. 8,44 Oxygen bubbles coalesce easier than H₂ bubbles in alkaline media, extending their sphere of influence and resulting in larger bubbles and longer lifetimes. As shown in Figure S18e, O₂ bubbles emerging from a plane on the cone architecture are as large as \sim 245 μ m, almost doubling the average size observed during the HER (Figure 4a). Moreover, the increased sphere of influence and greater O2 bubble coalescence might also explain why most of the studied geometries lacked significant differences between the plane and edge sites, resulting in more uniform bubble size and lifetime distributions. Round shapes (e.g., cones, rods) might favor the coalescence of bubbles growing next to each other, while distinct vertices and sharp turns (e.g., pyramids) prevent neighbor bubbles from coalescing and growing until detachment, resulting in longer lifetimes. These results demonstrate that bubble evolution characteristics of certain electrode architectures are also influenced by the evolving gas, and these factors must be considered when macroelectrodes are used.

2.4. OER Performance and Stability of 3D-Printed **Electrodes with Porous Architecture.** Providing robust and stable electrodes with large surface areas is essential for increasing the operational current density of water electrolyzers. Rather than using two-dimensional (2D) structures, 3D porous electrodes are ideal candidates for achieving this goal due to their large active surface area and improved mass transport. The current 3D substrate most commonly used for overall water splitting is commercial nickel foam (NF). While NF is porous, leading to increased active sites, its pores are randomly oriented throughout the structure. This disordered porous structure leads to significant bubble trapping, increasing the ohmic resistance and limiting the practical energy efficiency of the electrode. Inspired by Kou and co-workers, we examined the performance, bubble release, and OER stability of 3D-printed porous electrodes with ordered structure. Using this approach, we confirm (1) the robustness of our 3D printing-electrodeposition strategy to create 3D electrodes and that (2) periodic structures can, in addition to the electrode architectures discussed in Section 2.3, improve bubble release while resulting in satisfactory electrochemical performance. First, we examined the HER and OER performance of a Ni-coated 3D-printed porous electrode (Figure 6a) prepared following the same procedure as described in Section 2.1. Based on previous studies of a flow-through electrode, ^{6,7,16} the open, well-ordered porous structure for this electrode should facilitate bubble transport and suppress bubble coalescence.⁶ The exposed area of this porous electrode (regarded as 3D-Ni/Cu) is nearly six times larger than the planar electrode discussed in Sections 2.1 and 2.2 (Table S1). NCP and SEM images (Figures 6b,c and S19) reveal a rough surface covered by numerous protrusions (Figure 6b), confirming that our deposition methodology can also be applied to macroporous 3D electrodes. The electrochemical activity of the 3D-Ni/Cu electrode was evaluated from LSV scans over cathodic and anodic potentials in Fe-free 1.0 M KOH (Figure 6d). For HER, the 3D-Ni/Cu electrode required an overpotential of 133 mV to achieve a current density of -10 mA· cm⁻², and 202 mV to reach −50 mA·cm⁻². For OER, the electrode exhibited overpotentials of 400 and 512 mV at 10 and 50 mA·cm⁻², respectively. Notably, HER and OER activities of the 3D-Ni/Cu electrode are better than Ni foam (NF) and Cu foam (CF) control samples (Figure S20). We attribute this improved performance to the larger channel size of the 3D-Ni/

Cu electrode, which improves bubble release compared to the relatively small pore size of the NF, as reported by Kou et al. We also determined Tafel slopes of 80 and 123 mV·dec⁻¹ for HER and OER, respectively, with this electrode, which are comparable to the NF control sample (Figure S21), suggesting similar kinetics since the chemical composition was the same. We then compared the bubble release of the 3D-Ni/Cu electrode with commercial NF during the HER. Results are shown in Figure S22, and recordings are shown in Video V3. As displayed in Figure S22a, the bubble size distribution of the 3D-Ni/Cu electrode during HER at $-10 \text{ mA} \cdot \text{cm}^{-2}$ is comparable to the architectures studied in the previous section (Figure 4a). The large pore size of the 3D-Ni/Cu electrode prevents any bubble trapping inside the 3D structure, as the channels are well aligned with the upward movement of H2 bubbles due to buoyancy (see Video V3). Bubble trapping was also absent at higher current densities (−50 and −100 mA·cm⁻²), as shown in Figure S22b, confirming the efficient bubble removal without requiring electrolyte flow. In contrast to the 3D-Ni/Cu electrode, the NF sample exhibited larger bubbles and a broader size distribution (Figure S22c). At higher current densities, bubble trapping increased (see Video V3). The larger bubbles seen in the NF sample seem to be caused by the average pore size (\sim 250 μ m) and substantial coalescence inside the channels. Bubbles became trapped inside the random, porous skeleton when traveling upward due to buoyancy and experienced more collisions, thereby increasing bubble size and lifetime. Bubble trapping increases at higher current densities (Figure S22d), making it difficult to measure bubble diameters. Thereby, the 3D-Ni/Cu electrode effectively suppresses bubble trapping while also having the advantages of a large active surface area and high conductivity due to the thick Ni layer. Thus, 3D printing for controlled design of electrodes is highly advantageous, its main limitation being printing resolution, which limits the study of smaller pore sizes. Yet, pore size optimization of a similar 3Dprinted electrode has been already reported using a unique direct ink writing method.6

Maintaining OER stability is challenging due to the positive potentials that oxidize the Ni metal surface sites into a nickel oxide/hydroxide layer.²¹ OER cycling also induces structural changes due to the continuous reconstruction of layers exposed to the electrolyte, which increases the surface area and modifies material morphology. 45 Since our 3D-printed electrodes consist of sequential metallic layers (Figure 1d), characterizing the stability of the Ni coating and preventing the innermost Cu layer from being exposed to the electrolyte is essential. Hence, we examined the oxidation of our Ni-coated electrodes following long-term CV cycling in 1 M KOH. Sweeping the potential across the Ni^{2+/3+} redox peak activates the electrode until the response reaches a steady state, resulting in a stabilized form of the material (NiOOH) at anodic potentials.²⁸ Cycling the 3D porous electrode decreased the overpotential until stabilizing at around 300 and 398 mV at 10 and 50 mA·cm⁻², respectively (Figure 6f), which is caused by the formation of NiOOH sites. LSV scans before and after CV cycling illustrate this improvement (Figure 6d). Activity enhancement only occurred for OER, whereas a separate HER experiment resulted in stable activity (Figure 6d, dashed blue line).

To further measure the extent of oxidation and activity improvement, the electric charge associated with the Ni^{2+/3+} redox peak and the overpotential at 50 mA·cm⁻² were examined. The overpotential and charge stabilized at around 8000 cycles at ~398 mV and ~197 mC·cm⁻², respectively (Figure 6g),

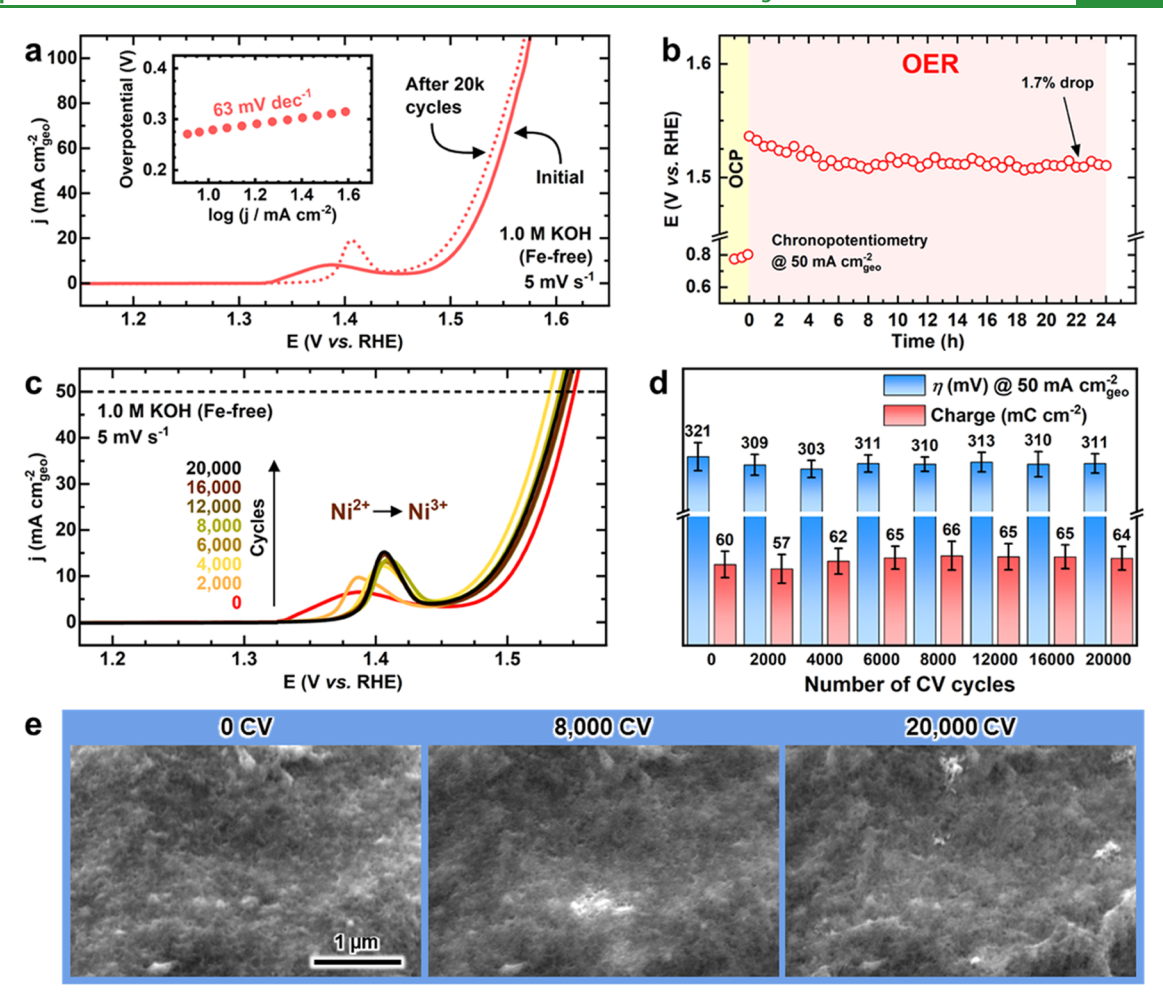


Figure 7. Characterization and evaluation of the NiFe/3D-Ni/Cu porous electrode: (a) OER polarization curves before (solid line) and after (dashed line) extended OER cycling (inset: Tafel slope), (b) chronopotentiometry test for 24 h at 50 mA·cm $^{-2}$, (c) evolution of the Ni $^{2+/3+}$ redox peak during extended OER cycling, (d) overpotential @ 50 mA·cm $^{-2}$ and charge of the Ni $^{2+/3+}$ redox peak variation during OER cycling, and (e) identical-location SEM images of the NiFe/3D-Ni/Cu porous electrode during OER cycling.

reaching a constant number of NiOOH sites. Note that sharpening of the Ni^{2+/3+} redox peak after 8000 cycles in Figure 6f can be explained by the increased ionic conductivity given by a thick α -Ni(OH)₂ layer with high structural order.⁴⁶ By periodically pausing CV activation to perform measurements and stabilize the electrode, the electrolyte effectively intercalated into the α -Ni(OH)₂ layer, resulting in rapid structural transformation. The $C_{\rm dl}$ also stabilized during activation (Figures S23 and S24). Note that in contrast to our previous ECSA estimations of pristine, nonoxidized samples (Sections 2.1 and 2.2) and under cathodic potentials (Figure S16), we did not use the standard specific capacitance of 40 μ F·cm⁻² to convert the C_{dl} into ECSA under OER conditions, since this value can vary with the composition of the oxide, resulting in misleading ECSA values.³⁵ Stabilization occurred after ~2000 cycles, which could be attributed to the larger surface area of the macroscopic scale 3D-Ni/Cu electrode. Nevertheless, these trends suggest that the number of OER active species (i.e., NiOOH) increases until stabilization occurs, resulting in a constant OER activity that lasts up to 20,000 cycles. We also documented surface morphology during the material activation by quasi-in situ SEM, i.e., pausing the experiment periodically to analyze the electrode. As shown in Figure 6h, the surface is eventually smoothed after 8000 cycles, and surface roughness and major protrusions are well maintained even after 20,000

cycles. EDX measurements to estimate the Ni/O ratio also confirmed the oxidation of the 3D-Ni/Cu electrode after OER, whereas the Ni/O ratio was nearly the same after HER (Figure S25). Cu redox signals were not detected in LSV scans (Figure 6f), and EDX spectra exhibited peaks only for Ni and O (Figure S25), suggesting that the Ni coating effectively protected the innermost Cu layer from oxidation. These results can be used to reduce the coating thickness, which is critical for optimizing the metal loading of commercial anodes.

2.5. Alkaline Water Electrolysis Tests Using NiFe-Coated 3D Porous Electrodes. Demonstrating the utility of 3D-printed electrodes as supports for electrocatalysts (with better activity than bare Ni) is also essential for improved electrolysis. Inspired by the approach of Ambrosi and Pumera comparing 3D-printed substrates with benchmark electrocatalysts, 19 we deposited NiFe composites on the surface of our 3D porous electrode and re-examined its performance. We adapted the electrodeposition approach reported by Lu and Zhao¹⁵ to grow mesoporous NiFe composites using our custom 3D-printed electrochemical flow cell, as previously reported by our group.²⁴ We characterized the composition of the resulting electrode (NiFe/3D-Ni/Cu) by XRD and X-ray photoelectron spectroscopy (XPS). Peaks from the XRD pattern were indexed to FeNi₃ (JCPDS No. 38-0419),^{47,48} as shown in Figure S26. Chemical composition was further examined via XPS,

demonstrating Ni 2p, Fe 2p, and O 1s spectral peaks for the pristine sample (Figure S27). The Ni 2p spectrum (Figure S27a) shows two spin-orbit peaks (i.e., Ni $2p_{1/2}$ and Ni $2p_{3/2}$) with a binding energy difference of 17.3 eV. Deconvoluted peaks can be assigned to Ni^{2+} (855.4 and 872.7 eV)⁴⁹⁻⁵¹ and satellites (~861 and ~878 eV),^{52,53} which are attributed to the presence of Ni(OH)₂. ^{28,49,54} The Fe 2p spectrum (Figure S27b) shows two spin-orbit peaks (i.e., Fe $2p_{1/2}$ and Fe $2p_{3/2}$) with a binding energy difference of 13.1 eV. Deconvoluted peaks can be assigned to Fe³⁺ (711.3 and 724.4 eV)^{50,55} and a satellite peak (\sim 718 eV),^{50,53} which is attributed to the presence of iron oxides/hydroxides. 15,21,53 We note that similar spectral shapes and binding energies of high-valent iron species make it difficult to assign species as FeOOH or Fe₂O₃. ^{50,56} Finally, deconvoluted peaks from the O 1s spectrum (Figure S27c) can be assigned to M-O(528.4 eV), ²¹ and $M-OH(530.6 \text{ eV})^{15,49}$ bonds and the peak at ~532 eV can be assigned to adsorbed water. 15,21 The presence of Ni²⁺, Fe³⁺, and lattice oxygen from XPS results suggests that the NiFe electrocatalytic layer has a layered double hydroxide structure. 21,55 Since no additional peaks in the XRD pattern were seen and no peaks for metallic Ni (\sim 852.6 eV)^{50,51} and Fe (\sim 705.5 eV)^{57,58} were detected, it is likely that the surface NiFe LDH layer is amorphous. 15,21

With an improved understanding of the composition, we next characterized the electrochemical performance of the NiFe/3D-Ni/Cu electrode. From LSV scans in the anodic region (Figure 7a), the NiFe/3D-Ni/Cu electrode requires overpotentials of 265 and 313 mV at 10 and 50 mA·cm⁻², respectively, with a Tafel slope of 63 mV·dec⁻¹. Overpotentials decrease to 250 and 306 mV at 10 and 50 mA·cm⁻², respectively, after CV activation. The activity of the NiFe/3D-Ni/Cu electrode lies within the range of previous NiFe double hydroxide electrocatalysts, including 3D-printed pyramid electrodes (258 mV at 10 mA· cm^{-2}), ²¹ NiFe/NF (215 mV at 10 mA·cm⁻²; 320 mV at 50 mA· cm⁻²), 15 and stainless steel meshes fabricated *via* selective laser melting metal printing (300 mV at 20 mA·cm⁻²). ¹⁹ After an initial stabilization drop of ~1.7%, the NiFe/3D-Ni/Cu electrode maintained an overpotential of ~280 mV when a constant current density of 50 mA·cm⁻² was applied for 24 h (Figure 7b). Over extended CV cycling (20,000 cycles), we find that the response stabilizes after 6000 cycles after a subtle overpotential decrease (Figures 7c,d and S28). The anodic shift of the Ni redox peak toward more positive potentials is attributed to changes in the electronic structure of the electrocatalyst, likely due to changes in Fe composition, according to previous studies. ^{28,59} A subtle increase in the Ni redox peak charge until stabilization around 65 mC·cm⁻² suggests a nearly constant number of active sites (Figure 7d). Furthermore, C_{dl} and R_{ct} values from EIS measurements stabilized after 6000 cycles (Figure S28), confirming the stabilization on the number of active sites. $C_{\rm dl}$ values from CV scans in the non-faradaic region also increased during CV cycling (Figure S29). Note that this trend is not completely reliable due to the loss of conductivity of surface oxides/ hydroxides generated during the OER, and use of EIS is recommended (Figure S28). SEM images taken at different cycling intervals confirmed subtle morphology changes (Figure 7e) caused by the surface oxidation, but major Ni microstructures and protrusions are well maintained (Figure S30). Surface oxidation was confirmed by EDX measurements (Figure S31), with O content increasing from 2.9 to 8.1% after 20,000 cycles with nearly invariant Ni and Fe content (Ni/Fe ratio \sim 3). EDX mapping further indicates that Ni and Fe were evenly

distributed over the surface after CV cycling (Figure S32). Identical XRD patterns after CV cycling confirm structural stability (Figure S33). XPS measurements after extended CV cycling (Figure S27) also revealed changes in the electronic structure and Ni/Fe oxidation states. Additional peaks emerged at ~856.8 and 874.1 eV (Figure S27a), broadening the total peak, as previously reported. These peaks can be assigned to Ni³⁺ (856.6 eV). The Fe 2p spectrum (Figure S27b) was deconvoluted into Fe³⁺ (711.3 and 724.4 eV). \$55,62 Finally, the O 1s spectrum (Figure S27c) showed an increase of the lattice oxygen peak, suggesting an increase in the Ni oxidation state after OER cycling. 24,60 These results confirm the surface oxidation of the NiFe LDH electrocatalyst into NiFe oxyhydroxide that acted as an OER active site.²¹

Based on previous studies regarding metal (e.g., Fe) incorporation/dissolution, we measured the elemental composition of the Fe-free KOH electrolyte using solutionmode inductively coupled plasma mass spectrometry (ICP-MS) to further confirm the electrode stability. By diluting the KOH matrix from samples taken at different time intervals, we determined the concentration of elements and monitored their changes during CV cycling (Scheme S3, for experimental details, see the Supporting Information). As expected, the Fe concentration remained below the detection limit (i.e., 0.24 ppb, Figure S34) since we only utilized Fe-free KOH electrolyte (Table S3). However, Ni and Mn concentrations in the electrolyte decreased suddenly after 2000 cycles, suggesting metal redeposition onto the electrocatalyst until surface stabilization was reached (Figure S35). The concentration of other elements in the KOH electrolyte (e.g., Ca, K, Na, Al, Si, Zn, Co, Rb, and Mo) remained constant or was below the detection limit (Table S3), suggesting that selective Ni and Mn redeposition occurred, which could explain the subtle changes in the electronic structure and activity enhancement until stabilization was completed. 63-65 Thus, this redeposition/ incorporation process requires further investigation to truly determine if redeposition/incorporation could be a contributing factor to electrocatalytic activity enhancement with increasing CV cycling number.

3. CONCLUSIONS

In summary, we have demonstrated that tuning extrinsic electrode properties (i.e., surface properties and the electrode architecture) using 3D printing and facile deposition methods provides a versatile, reproducible, and effective way to characterize electrochemical performance and bubble release. We engineered robust and cost-effective electrodes through a combined SLS 3D printing and metal deposition approach, resulting in several beneficial properties, including strong coating adhesion, large surface area, high wettability, fast charge transfer, and good stability in alkaline media. Using different techniques combined with a systematic statistical approach, we examined the impact of HBT Ni electrodeposition conditions on key extrinsic properties, confirming the close relationship between these properties and the electrochemical performance and providing valuable guidelines for optimization and surface engineering of electrodes. Furthermore, by testing different electrode architectures, we demonstrated the relevance of electrode geometry, feature size, and electrolyte flow rate on bubble release. We found that geometric edges limit the bubble release as these result in large bubbles with long lifetimes. However, this edge effect can be diminished using electrode architectures with tilted, curved, and rough macroscopic features

(e.g., cone and oval patterns), decreasing the size of these features (i.e., micron-sized architectures) or pumping the electrolyte at a certain flow rate. How our findings apply to electrode architectures of different shapes and scales will require further investigation, but our results demonstrate the importance of studying electrode geometry as a crucial parameter for designing and fabricating electrodes, which is critical for practical high current density application. Our approach combines the advantages of effective macroscopic architectures and precise surface engineering for making highperformance electrodes without altering intrinsic electrocatalytic activity. By testing the 3D porous architecture under highly oxidizing OER conditions, we also confirmed the stability of our electrodes fabricated via 3D printing—electrodeposition. We experimentally demonstrated the effectiveness of this electrode architecture as a support for NiFe electrocatalysts with large surface area and intrinsic catalytic activity comparable to similar works in the literature. Further rigorous tests of Ni/ Cu-coated supports, gas bubble transport efficiencies of different architectures, and electronic effects due to metal incorporation are needed. From a broader view, these results confirm that engineering 3D-printed electrodes with tunable properties offers a convenient approach for performing precise, reproducible, and controllable electrochemistry experiments at the lab scale.

4. EXPERIMENTAL SECTION

4.1. Materials. Sodium hydroxide, trisodium phosphate, sodium carbonate, sodium dodecyl sulfate, sodium silicate, sodium thiosulfate, potassium sodium tartrate, potassium ferrocyanide, potassium permanganate, sulfuric acid, hydrochloric acid, acetic acid, ethanol, and copper sulfate were purchased from Fisher Scientific. Nickel chloride, nickel sulfate, and nickel and copper foils (500 μ m thick) were purchased from Alfa Aesar. Potassium hydroxide (90 wt % pure), ethylenediaminetetraacetic acid (EDTA) disodium, 2,2'-dipyridyl, and silver nitrate were purchased from Sigma-Aldrich. Epoxy resin (Superclear 2.0) was purchased from Fiberglass Coatings, Inc. Nickel foam (99.99%, 80-110 pores per inch, 1.6 mm thick) and Cu foam (99.99%, porosity 70-80%, 0.08 mm thick) were purchased from MTI Co. Nylon 12 grey powder and clear resin for 3D printing were purchased from Formlabs. All aqueous solutions were prepared with deionized water (18 M Ω). Notably, the KOH electrolyte was purified through a previously reported method^{24,28,59} to avoid incidental activity enhancement due to Fe impurities during OER tests. We also examined our electrolytes during testing via ICP-MS to detect any impurities that could be released by 3D-printed components and to monitor potential metal dissolution to gauge electrode stability.

4.2. 3D Printing of Nylon Substrates. Electrode designs were conceived in SolidWorks 2020 (Dassault Systemes). The 3D models were exported as .stl files and printed using a Fuse 1 printer (Formlabs), which uses high-performance selective laser sintering (SLS) 3D printing technology. Electrodes were printed using a layer thickness of 110 μ m and an ytterbium fiber laser (1064 nm, 10 W) with a laser spot size of 200 μ m and a material refresh rate of 30%. All electrodes were printed with nylon 12 grey powder (Formlabs FLP12G01). Nylon 12 samples exhibit a tensile strength of 50 MPa, elongation at failure of 6–11%, and good environmental stability in water (absorption: 0.66%) and alkaline media (wt % gain <0.2% in NaOH at pH 10, after 24 h of immersion) according to the manufacturer's data sheet.

4.3. 3D Printing of Electrolyzer Frames. 3D-printed components of the electrochemical cell were designed using SolidWorks software. All 3D models were exported as .stl files and printed using a Form 3 printer (Formlabs), which uses SLA 3D printing technology. Components were printed using a layer thickness of 50 μ m and a 405 nm laser diode (250 mW) with a laser spot size of 85 μ m. All electrolyzer components were printed with clear resin (Formlabs FLGPCL04). According to the manufacturer, samples exhibit a tensile strength of 38 MPa, elongation at failure of 12%, and environmental

stability in water (absorption: <1%) and alkaline media (wt % gain <1% in NaOH at pH 10, after 24 h of immersion).

4.4. Deposition of Metallic Films on 3D-Printed Substrates. The sequential deposition approach was adapted from previous studies. First, a thin Cu layer was deposited onto nylon substrates through an electroless deposition method reported by Wang et al.²⁵ The detailed Cu electroless deposition procedure and detailed solution compositions are depicted in Scheme S4. Substrates were degreased using a cleaning solution and then cleaned by ultrasonic washing in deionized water. Samples were dried overnight at room temperature. Then, a thin layer of epoxy resin was applied with a clean brush. Substrates were tilted $\sim 30^{\circ}$ for 24 h to remove the excess. The epoxy-coated substrates were degreased and washed with deionized water again. The surface was then oxidized by immersing the piece into a KMnO₄ solution, followed by deionized water rinsing. Subsequently, the surface was activated by immersing the piece into a sodium thiosulfate solution. Afterward, the electrode was immersed into a silver nitrate solution, and then the pieces were immersed in deionized water for 24 h. Next, electroless copper plating was performed for 40 min in a copper sulfate and formaldehyde bath. Cu-coated electrodes were rinsed with copious amounts of water and dried under vacuum.

After Cu deposition, the electrodes were coated with nickel through an electrodeposition procedure adapted from earlier methods by Shin and Liu⁶⁷ and our previous work. ²³ Ni electrodeposition was performed in a custom plating cell designed so that distances between electrodes were always the same (Figure S36). As depicted in Scheme S5, the Ni layer consisted of sequential Ni deposition steps, each providing different degrees of roughness. First, a thin, relatively smooth Ni coating (Ni-P, P: planar) was deposited by immersing the Cu-coated substrate into a Woods strike bath at a low current density of $-70 \text{ mA} \cdot \text{cm}^{-2}$ for 90 s. Then, additional Ni layers were deposited, following the HBT electrodeposition method. First, the Ni, Cu-coated electrode was immersed in a 0.5 M NiSO₄ plating bath at a high current density of 0.8 A·cm⁻² for 30 s (charge: 300 C). Immediately afterward, the electrode was immersed in a 50 mM NiSO₄ plating bath at a high current density of 0.8 A·cm⁻² for 20 s (charge: 200 C). Finally, the electrodes were immersed in deionized water for 12 h, dried with compressed air, and stored in a vacuum oven. Detailed plating bath compositions and procedures are shown in the Supporting Information.

NiFe plating was performed using the optimized conditions reported by Lu and Zhao. 15 As demonstrated by our previous works, 23,24 utilized a custom 3D-printed electrochemical flow cell to improve the mass transfer and electrolyte mixing during electrodeposition. This cell configuration also provided a constant electrode spacing of 5 mm, improving reproducibility. The plating bath consisted of a mixture of 3 mM $Ni(NO_3)_2 \cdot 6H_2O$ and 3 mM $Fe(NO_3)_3 \cdot 9H_2O$ $(Ni^{2+}/Fe^{3+}$ molar ratio: 1:1). Electrodeposition was performed at a constant potential of -1.0 V (vs Ag/AgCl) for 5 min while the plating bath was recirculated at a flow rate of 250 mL·min⁻¹. Afterward, the new NiFe/3D-Ni/Cu electrodes were rinsed with deionized water and ethanol, dried in air, and stored under vacuum.

4.5. Physicochemical Characterization. The crystallinity of the SLS substrates and metal coatings in the range from 20 to 80 2θ degree was assessed by XRD using a Rigaku MiniFlex 600 X-ray diffractometer equipped with a Cu source. A 3D-printed sample holder equipped with a B-doped Si plate (MTI Co.) was utilized to eliminate external contributions from bulk XRD measurements. GIXRD patterns were measured using an ULTIMA IV diffractometer at a speed of 0.5° ⋅ min⁻¹ and $\omega = 0.3^{\circ}$. The surface roughness of the electrodes was measured by NCP using a Keyence VK-X1100 optical profilometer. High-quality surface images at different magnifications were taken using the focus variation and laser confocal modes. For capturing SEM images of the nonconductive 3D-printed architecture, nylon substrates were coated with a thin (~5 nm) layer of a Pd/Au layer (40:60, density: 16.40 g· cm⁻³) at a current of 30 mA for 30 s using an EMS sputter coater. For collecting cross-sectional images, the electrodes were coated with a layer of silver conductive epoxy (Ted Pella, Inc.), kept under vacuum overnight, and then cut with a razor blade. The contact angle was measured by placing a water droplet on the surface of the planar electrodes using a First Ten Ångstroms FTA-200 contact angle

goniometer. Live recordings (1080P HD at 30 fps) of bubble evolution tests were captured using a TOMLOV digital microscope (2 MP, 50-2000× zoom, spatial resolution: \sim 4 μ m per pixel) when the electrode was placed inside the custom visualization cell depicted in Figure S11. Bubble diameter and lifetime analyses from recordings were done as follows: recordings were inspected until a random bubble was located on the electrode surface. Each bubble was tracked frame by frame to measure (1) the time from noticeable nucleation until detachment from the surface (i.e., bubble lifetime) and (2) the maximum bubble diameter at detachment. Bubble diameters were estimated by saving a highquality snapshot and drawing a line across the bubble using ImageJ software. For bubble evolution studies on micro-sized features using the non-contact profilometer (Figure 5), the circle measurement tool of Keyence's Multi-File Analyzer software was utilized. This procedure was repeated for 50 different bubbles chosen randomly to construct bubble size and lifetime histograms. For controlled flow studies, the electrolyte was pumped using a Stenner 85M5 series peristaltic metering pump at a constant flow rate of 250 mL·min⁻¹. The morphology of the materials was examined by SEM using a FEI Quanta 650 environmental scanning electron microscope. For quasi-in situ measurements, the exact location was monitored through SEM at different intervals during CV cycling. Here, the electrodes were retrieved from the cell and dried in a vacuum oven for 12 h before SEM imaging. EDX was utilized to obtain elemental mappings of top-view and cross-sectional SEM images of the electrodes. XPS was employed to investigate surface chemical composition using a Kratos AXIS Ultra DLD spectrometer. A monochromatic Al K α X-ray source (hv = 1486.6eV) was utilized for studying the 3D-printed electrodes. For NiFe electrodes, surface composition was obtained using a Mg Ka X-ray source (hv = 1253.6 eV) with a spot size of $300 \times 700 \text{ mm}^2$. The binding energies of Ni 2p, Fe 2p, Cu 2p, Cu LMM, and O 1s were corrected/ verified with the C 1s major peak of adventitious carbon at 284.8 eV. XPS data were processed using CasaXPS software. Electrolyte composition was examined through solution-mode ICP-MS using an Agilent 7500ce equipped with a collision reaction cell (He and H₂ modes). For analyzing challenging KOH electrolyte samples, we devised a procedure that is detailed in the Supporting Information.

4.6. Electrochemical Measurements. Electrochemical tests were performed in our custom electrochemical cell with a parallel plate configuration depicted in Scheme S6 and Figure S37. Electrodes were placed in position, and then the cell was assembled using proper sealing gaskets and stainless steel bolts, as detailed in our previous work. Electrochemical tests were conducted using a CHI660D electrochemical workstation (CH Instrument) with a three-electrode configuration. All measurements were performed in Fe-free 1.0 M KOH using a Hg/HgO reference electrode with the same electrolyte as filling solution (CH Instruments). Potentials were converted to the reversible hydrogen electrode (RHE) according to the equation ($E_{\rm RHE} = E_{\rm Hg/HgO}^{\circ} + 0.0592 \times {\rm pH} + E_{\rm Hg/HgO}, E_{\rm Hg/HgO}^{\circ} (1.0 {\rm M~KOH}) = 0.11 {\rm V}$ at 25 °C). Unless specified otherwise, a graphite rod was always utilized as the counter electrode to avoid incidental Pt incorporation. The *iR* drop was compensated by 85% for all CV and LSV measurements.

CV scans of planar Cu and Ni electrodes were recorded at a scan rate of 50 mV·s⁻¹. LSV scans of electrodes with different architectures were recorded at a scan rate of 1 mV·s⁻¹. The ECSA was estimated through the double-layer capacitance $(C_{\rm dl})$ method.⁶⁹ The latter was estimated from CV scans (at ±50 mV around the OCP) recorded from 200 to 10 mV·s⁻¹. Cathodic and anodic currents in the middle of the potential window were averaged and plotted against the scan rate, giving the linear behavior of an ideal capacitor. The slope of the fitted line was associated with the value of $C_{\text{d}\nu}$ which was compared between electrodes. The ECSA was estimated as the ratio of the $C_{\rm dl}$ and $C_{\rm s}$ for a metal surface $(40 \,\mu\text{F}\cdot\text{cm}^{-2})$. Roughness factors were estimated as the ratio of the ECSA and the exposed area calculated from 3D models $\,$ (Table S1). Tafel slopes were calculated from LSV curves using the Tafel equation: $\eta = a + b \log |j|$, where η represents the overpotential, b is the Tafel slope, a is a constant, and j is the current density. EIS tests were performed to find the R_{ct} of the as-prepared electrodes. EIS was measured in the frequency range from 10⁻² to 10⁶ Hz with 10 mV of amplitude. For planar electrodes in Sections 2.1 and 2.2, the HER was

probed at -0.05 V vs RHE. For 3D porous electrodes in Sections 2.4 and 2.5, OER was probed at 1.5 V vs RHE. EIS fitting was performed using the general Randles equivalent circuit model, and fitted parameters were determined using ZView software (Scribner Associates). LSV scans at different periods were recorded during prolonged CV cycling around the Ni^{2+/3+} redox peak (from 1.24 to 1.54 V vs RHE). The overpotential at 50 mA·cm⁻² and the charge of the Ni^{2+/3+} redox peak (based on the area under the curve) were monitored during CV cycling to evaluate OER stability of the 3D porous electrodes (Ni and NiFe surfaces). Additionally, the stability of the NiFe 3D porous electrode during OER tests was assessed through CP runs during 24 h at 50 mA·cm⁻².

ASSOCIATED CONTENT

Supporting Information

The Supporting Information is available free of charge at https://pubs.acs.org/doi/10.1021/acsami.2c12579.

Additional electrochemical and physicochemical characterization results, schematic illustrations of experimental procedures, pictures of experimental setups, statistical analysis results, bubble evolution videos, bubble evolution histograms, and ICP-MS analysis details (PDF)

Recordings of bubble evolution tests under stagnant conditions (Video V1) (MP4)

Recordings of bubble evolution tests under controlled flow rate (Video V2) (MP4)

Recordings of a comparison of the bubble release of the 3D-Ni/Cu electrode with commercial NF during the HER (Video V3) (MP4)

AUTHOR INFORMATION

Corresponding Author

C. Buddie Mullins — Department of Chemistry, The University of Texas at Austin, Austin, Texas 78712, United States; McKetta Department of Chemical Engineering, Texas Materials Institute, Center for Electrochemistry, and H2@UT, The University of Texas at Austin, Austin, Texas 78712, United States; Orcid.org/0000-0003-1030-4801; Email: mullins@che.utexas.edu

Authors

Raúl A. Márquez — Department of Chemistry, The University of Texas at Austin, Austin, Texas 78712, United States;
orcid.org/0000-0003-3885-5007

Kenta Kawashima — Department of Chemistry, The University of Texas at Austin, Austin, Texas 78712, United States;
orcid.org/0000-0001-7318-6115

Yoon Jun Son – McKetta Department of Chemical Engineering, The University of Texas at Austin, Austin, Texas 78712, United States; orcid.org/0000-0003-1704-2314

Roger Rose — Texas Inventionworks, The University of Texas at Austin, Austin, Texas 78712, United States

Lettie A. Smith — Department of Chemistry, The University of Texas at Austin, Austin, Texas 78712, United States;
ocid.org/0000-0003-0378-072X

Nathaniel Miller – Department of Geosciences, The University of Texas at Austin, Austin, Texas 78712, United States

Omar Ali Carrasco Jaim — McKetta Department of Chemical Engineering, The University of Texas at Austin, Austin, Texas 78712, United States

Hugo Celio — Texas Materials Institute, The University of Texas at Austin, Austin, Texas 78712, United States

Complete contact information is available at:

https://pubs.acs.org/10.1021/acsami.2c12579

Author Contributions

The manuscript was written through contributions by all authors. All authors have approved the final version of the manuscript.

Notes

The authors declare no competing financial interest.

ACKNOWLEDGMENTS

R.A.M., K.K., Y.J.S., L.A.S., and C.B.M. gratefully acknowledge funding from the National Science Foundation (NSF) *via* Grants CHE-1664941 and CHE-2102307, and the Welch Foundation through Grant F-1436 for their generous support. We also acknowledge the assistance from the Texas Inventionworks staff, particularly Roger Rose, Steve Ferraro, and Scott Evans, for fabricating the 3D-printed components.

REFERENCES

- (1) Jacobson, M. Z. Review of Solutions to Global Warming, Air Pollution, and Energy Security. *Energy Environ. Sci.* **2009**, *2*, 148–173.
- (2) Jacobsson, T. J.; Fjallstrom, V.; Edoff, M.; Edvinsson, T. Sustainable Solar Hydrogen Production: From Photoelectrochemical Cells to PV-Electrolyzers and Back Again. *Energy Environ. Sci.* **2014**, *7*, 2056–2070.
- (3) Chen, Z.; Duan, X.; Wei, W.; Wang, S.; Ni, B.-J. Recent Advances in Transition Metal-Based Electrocatalysts for Alkaline Hydrogen Evolution. *J. Mater. Chem. A* **2019**, *7*, 14971–15005.
- (4) Davis, S. J.; Lewis, N. S.; Shaner, M.; Aggarwal, S.; Arent, D.; Azevedo, I. L.; Benson, S. M.; Bradley, T.; Brouwer, J.; Chiang, Y.-M.; Clack, C. T. M.; Cohen, A.; Doig, S.; Edmonds, J.; Fennell, P.; Field, C. B.; Hannegan, B.; Hodge, B.-M.; Hoffert, M. I.; Ingersoll, E.; Jaramillo, P.; Lackner, K. S.; Mach, K. J.; Mastrandrea, M.; Ogden, J.; Peterson, P. F.; Sanchez, D. L.; Sperling, D.; Stagner, J.; Trancik, J. E.; Yang, C.-J.; Caldeira, K. Net-Zero Emissions Energy Systems. *Science* 2018, 360, No. eaas9793.
- (5) Schmidt, O.; Gambhir, A.; Staffell, I.; Hawkes, A.; Nelson, J.; Few, S. Future Cost and Performance of Water Electrolysis: An Expert Elicitation Study. *Int. J. Hydrogen Energy* **2017**, 42, 30470–30492.
- (6) Kou, T.; Wang, S.; Shi, R.; Zhang, T.; Chiovoloni, S.; Lu, J. Q.; Chen, W.; Worsley, M. A.; Wood, B. C.; Baker, S. E.; Duoss, E. B.; Wu, R.; Zhu, C.; Li, Y. Periodic Porous 3D Electrodes Mitigate Gas Bubble Traffic during Alkaline Water Electrolysis at High Current Densities. *Adv. Energy Mater.* **2020**, *10*, No. 2002955.
- (7) Yang, F.; Kim, M. J.; Brown, M.; Wiley, B. J. Alkaline Water Electrolysis at 25 A Cm-2 with a Microfibrous Flow-through Electrode. *Adv. Energy Mater.* **2020**, *10*, No. 2001174.
- (8) Zhao, X.; Ren, H.; Luo, L. Gas Bubbles in Electrochemical Gas Evolution Reactions. *Langmuir* **2019**, *35*, 5392–5408.
- (9) Xu, W.; Lu, Z.; Sun, X.; Jiang, L.; Duan, X. Superwetting Electrodes for Gas-Involving Electrocatalysis. *Acc. Chem. Res.* **2018**, *51*, 1590–1598.
- (10) Kim, B. K.; Kim, M. J.; Kim, J. J. Impact of Surface Hydrophilicity on Electrochemical Water Splitting. *ACS Appl. Mater. Interfaces* **2021**, 13, 11940–11947.
- (11) Iwata, R.; Zhang, L.; Wilke, K. L.; Gong, S.; He, M.; Gallant, B. M.; Wang, E. N. Bubble Growth and Departure Modes on Wettable/Non-Wettable Porous Foams in Alkaline Water Splitting. *Joule* **2021**, *5*, 887–900
- (12) Angulo, A.; van der Linde, P.; Gardeniers, H.; Modestino, M.; Fernández Rivas, D. Influence of Bubbles on the Energy Conversion Efficiency of Electrochemical Reactors. *Joule* **2020**, *4*, 555–579.
- (13) Pham, T. N.; Sharifi, T.; Sandström, R.; Siljebo, W.; Shchukarev, A.; Kordas, K.; Wågberg, T.; Mikkola, J.-P. Robust Hierarchical 3D Carbon Foam Electrode for Efficient Water Electrolysis. *Sci. Rep.* **2017**, 7, No. 6112.

- (14) Pérez-Alonso, F.; Adán, C.; Rojas, S.; Peña, M. A.; Fierro, J. L. G. Ni/Fe Electrodes Prepared by Electrodeposition Method over Different Substrates for Oxygen Evolution Reaction in Alkaline Medium. *Int. J. Hydrogen Energy* **2014**, *39*, 5204–5212.
- (15) Lu, X.; Zhao, C. Electrodeposition of Hierarchically Structured Three-Dimensional Nickel—Iron Electrodes for Efficient Oxygen Evolution at High Current Densities. *Nat. Commun.* **2015**, *6*, No. 6616.
- (16) Arenas, L. F.; Ponce de León, C.; Walsh, F. C. Three-Dimensional Porous Metal Electrodes: Fabrication, Characterisation and Use. *Curr. Opin. Electrochem.* **2019**, *16*, 1–9.
- (17) Ambrosi, A.; Shi, R. R. S.; Webster, R. D. 3D-Printing for Electrolytic Processes and Electrochemical Flow Systems. *J. Mater. Chem. A* **2020**, *8*, 21902–21929.
- (18) Hu, L.; Jiang, G. 3D Printing Techniques in Environmental Science and Engineering Will Bring New Innovation. *Environ. Sci. Technol.* **2017**, *51*, 3597–3599.
- (19) Ambrosi, A.; Pumera, M. Multimaterial 3D-Printed Water Electrolyzer with Earth-Abundant Electrodeposited Catalysts. *ACS Sustainable Chem. Eng.* **2018**, *6*, 16968–16975.
- (20) Ambrosi, A.; Pumera, M. 3D-Printing Technologies for Electrochemical Applications. *Chem. Soc. Rev.* **2016**, *45*, 2740–2755.
- (21) Ahn, J.; Park, Y. S.; Lee, S.; Yang, J.; Pyo, J.; Lee, J.; Kim, G. H.; Choi, S. M.; Seol, S. K. 3D-Printed NiFe-Layered Double Hydroxide Pyramid Electrodes for Enhanced Electrocatalytic Oxygen Evolution Reaction. *Sci. Rep.* **2022**, *12*, No. 346.
- (22) Paul, M. T. Y.; Yee, B. B.; Bruce, D. R.; Gates, B. D. Hexagonal Arrays of Cylindrical Nickel Microstructures for Improved Oxygen Evolution Reaction. *ACS Appl. Mater. Interfaces* **2017**, *9*, 7036–7043.
- (23) Márquez-Montes, R. A.; Collins-Martínez, V. H.; Pérez-Reyes, I.; Chávez-Flores, D.; Graeve, O. A.; Ramos-Sánchez, V. H. Electrochemical Engineering Assessment of a Novel 3D-Printed Filter-Press Electrochemical Reactor for Multipurpose Laboratory Applications. ACS Sustainable Chem. Eng. 2020, 8, 3896—3905.
- (24) Marquez-Montes, R. A.; Kawashima, K.; Son, Y. J.; Weeks, J. A.; Sun, H. H.; Celio, H.; Ramos-Sánchez, V. H.; Mullins, C. B. Mass Transport-Enhanced Electrodeposition of Ni–S–P–O Films on Nickel Foam for Electrochemical Water Splitting. *J. Mater. Chem. A* **2021**, *9*, 7736–7749.
- (25) Wang, Y.; Ni, L.; Yang, F.; Gu, F.; Liang, K.; Marcus, K.; Wan, Y.; Chen, J.; Feng, Z. Facile Preparation of a High-Quality Copper Layer on Epoxy Resin via Electroless Plating for Applications in Electromagnetic Interference Shielding. *J. Mater. Chem. C* **2017**, *5*, 12769–12776.
- (26) Chang, Y.; Tao, Y.; Zhang, Q.; Yang, Z.-G. Selective Adsorption of Catalyst and Copper Plating for Additive Fabrication of Conductive Patterns and Through-Holes. *Electrochim. Acta* **2015**, *158*, 7–12.
- (27) Huang, L.-F.; Hutchison, M. J.; Santucci, R. J.; Scully, J. R.; Rondinelli, J. M. Improved Electrochemical Phase Diagrams from Theory and Experiment: The Ni–Water System and Its Complex Compounds. J. Phys. Chem. C 2017, 121, 9782–9789.
- (28) Son, Y. J.; Kawashima, K.; Wygant, B. R.; Lam, C. H.; Burrow, J. N.; Celio, H.; Dolocan, A.; Ekerdt, J. G.; Mullins, C. B. Anodized Nickel Foam for Oxygen Evolution Reaction in Fe-Free and Unpurified Alkaline Electrolytes at High Current Densities. *ACS Nano* **2021**, *15*, 3468
- (29) Plowman, B. J.; Jones, L. A.; Bhargava, S. K. Building with Bubbles: The Formation of High Surface Area Honeycomb-like Films via Hydrogen Bubble Templated Electrodeposition. *Chem. Commun.* **2015**, *51*, 4331–4346.
- (30) Giri, S. D.; Sarkar, A. Electrochemical Study of Bulk and Monolayer Copper in Alkaline Solution. *J. Electrochem. Soc.* **2016**, *163*, H252.
- (31) Shalom, M.; Ressnig, D.; Yang, X.; Clavel, G.; Fellinger, T. P.; Antonietti, M. Nickel Nitride as an Efficient Electrocatalyst for Water Splitting. *J. Mater. Chem. A* **2015**, *3*, 8171–8177.
- (32) Ma, N.; Liu, W.; Ma, L.; He, S.; Liu, H.; Zhang, Z.; Sun, A.; Huang, M.; Zhu, C. Crystal Transition and Thermal Behavior of Nylon 12. *e-Polymers* **2020**, *20*, 346–352.

- (33) McCrory, C. C. L.; Jung, S.; Peters, J. C.; Jaramillo, T. F. Benchmarking Heterogeneous Electrocatalysts for the Oxygen Evolution Reaction. *J. Am. Chem. Soc.* **2013**, *135*, 16977–16987.
- (34) Yoon, Y.; Yan, B.; Surendranath, Y. Suppressing Ion Transfer Enables Versatile Measurements of Electrochemical Surface Area for Intrinsic Activity Comparisons. *J. Am. Chem. Soc.* **2018**, *140*, 2397–2400.
- (35) Mefford, J. T.; Akbashev, A. R.; Zhang, L.; Chueh, W. C. Electrochemical Reactivity of Faceted β -Co(OH)2 Single Crystal Platelet Particles in Alkaline Electrolytes. *J. Phys. Chem. C* **2019**, *123*, 18783–18794.
- (36) Hao, J.; Yang, W.; Huang, Z.; Zhang, C. Superhydrophilic and Superaerophobic Copper Phosphide Microsheets for Efficient Electrocatalytic Hydrogen and Oxygen Evolution. *Adv. Mater. Interfaces* **2016**, 3, No. 1600236.
- (37) Zhang, Q.; Li, T.; Liang, J.; Wang, N.; Kong, X.; Wang, J.; Qian, H.; Zhou, Y.; Liu, F.; Wei, C.; Zhao, Y.; Zhang, X. Highly Wettable and Metallic NiFe-Phosphate/Phosphide Catalyst Synthesized by Plasma for Highly Efficient Oxygen Evolution Reaction. *J. Mater. Chem. A* **2018**, *6*, 7509–7516.
- (38) Zhang, J.; Dong, F.; Wang, C.; Wang, J.; Jiang, L.; Yu, C. Integrated Bundle Electrode with Wettability-Gradient Copper Cones Inducing Continuous Generation, Directional Transport, and Efficient Collection of H2 Bubbles. ACS Appl. Mater. Interfaces 2021, 13, 32435–32441.
- (39) Fayzi, P.; Bastani, D.; Lotfi, M.; Khararoodi, M. G. The Effects of Bubble Detachment Shape on Rising Bubble Hydrodynamics. *Sci. Iran.* **2019**, *26*, 1546–1554.
- (40) Hao, R.; Fan, Y.; Howard, M. D.; Vaughan, J. C.; Zhang, B. Imaging Nanobubble Nucleation and Hydrogen Spillover during Electrocatalytic Water Splitting. *Proc. Natl. Acad. Sci. U.S.A.* **2018**, *115*, 5878–5883.
- (41) Eigeldinger, J.; Vogt, H. The Bubble Coverage of Gas-Evolving Electrodes in a Flowing Electrolyte. *Electrochim. Acta* **2000**, *45*, 4449–4456.
- (42) Han, B.; Stoerzinger, K. A.; Tileli, V.; Gamalski, A. D.; Stach, E. A.; Shao-Horn, Y. Nanoscale Structural Oscillations in Perovskite Oxides Induced by Oxygen Evolution. *Nat. Mater* **2017**, *16*, 121–126.
- (43) Skorb, E. V.; Möhwald, H.; Andreeva, D. V. Effect of Cavitation Bubble Collapse on the Modification of Solids: Crystallization Aspects. *Langmuir* **2016**, 32, 11072–11085.
- (44) Janssen, L. J. J.; Sillen, C. W. M. P.; Barendrecht, E.; van Stralen, S. J. D. Bubble Behaviour during Oxygen and Hydrogen Evolution at Transparent Electrodes in KOH Solution. *Electrochim. Acta* **1984**, *29*, 633–642.
- (45) Deng, J.; Nellist, M. R.; Stevens, M. B.; Dette, C.; Wang, Y.; Boettcher, S. W. Morphology Dynamics of Single-Layered Ni(OH)2/NiOOH Nanosheets and Subsequent Fe Incorporation Studied by in Situ Electrochemical Atomic Force Microscopy. *Nano Lett.* **2017**, *17*, 6922–6926.
- (46) Hall, D. S.; Bock, C.; MacDougall, B. R. An Oxalate Method for Measuring the Surface Area of Nickel Electrodes. *J. Electrochem. Soc.* **2014**, *161*, H787.
- (47) Abellán, G.; Carrasco, J. A.; Coronado, E.; Prima-García, H. Synthesis of FeNi3 Nanoparticles in Benzyl Alcohol and Their Electrical and Magnetic Properties. *J. Sol–Gel Sci. Technol.* **2014**, *70*, 292–299.
- (48) Jia, J.; Yu, J. C.; Wang, Y.-X. J.; Chan, K. M. Magnetic Nanochains of FeNi3 Prepared by a Template-Free Microwave-Hydrothermal Method. *ACS Appl. Mater. Interfaces* **2010**, *2*, 2579–2584.
- (49) Weidler, N.; Schuch, J.; Knaus, F.; Stenner, P.; Hoch, S.; Maljusch, A.; Schäfer, R.; Kaiser, B.; Jaegermann, W. X-Ray Photoelectron Spectroscopic Investigation of Plasma-Enhanced Chemical Vapor Deposited NiOx, NiOx(OH)y, and CoNiOx(OH)y: Influence of the Chemical Composition on the Catalytic Activity for the Oxygen Evolution Reaction. *J. Phys. Chem. C* 2017, 121, 6455–6463.
- (50) Biesinger, M. C.; Payne, B. P.; Grosvenor, A. P.; Lau, L. W. M.; Gerson, A. R.; Smart, R. S. C. Resolving Surface Chemical States in XPS

- Analysis of First Row Transition Metals, Oxides and Hydroxides: Cr, Mn, Fe, Co and Ni. Appl. Surf. Sci. 2011, 257, 2717–2730.
- (51) Grosvenor, A. P.; Biesinger, M. C.; Smart, R. S. C.; McIntyre, N. S. New Interpretations of XPS Spectra of Nickel Metal and Oxides. *Surf. Sci.* **2006**, *600*, 1771–1779.
- (52) Kim, J.-H.; Youn, D. H.; Kawashima, K.; Lin, J.; Lim, H.; Mullins, C. B. An Active Nanoporous Ni(Fe) OER Electrocatalyst via Selective Dissolution of Cd in Alkaline Media. *Appl. Catal., B* **2018**, 225, 1–7.
- (53) Pan, Y.; Wu, Y.; Hsain, H. A.; Su, R.; Cazorla, C.; Chu, D. Synergetic Modulation of the Electronic Structure and Hydrophilicity of Nickel—Iron Hydroxide for Efficient Oxygen Evolution by UV/Ozone Treatment. J. Mater. Chem. A 2020, 8, 13437—13442.
- (54) Kawashima, K.; Márquez-Montes, R. A.; Li, H.; Shin, K.; Cao, C. L.; Vo, K. M.; Son, Y. J.; Wygant, B. R.; Chunangad, A.; Youn, D. H.; Henkelman, G.; Ramos-Sánchez, V. H.; Mullins, C. B. Electrochemical Behavior of a Ni3N OER Precatalyst in Fe-Purified Alkaline Media: The Impact of Self-Oxidation and Fe Incorporation. *Mater. Adv.* 2021, 2, 2299.
- (55) Cai, Z.; Zhou, D.; Wang, M.; Bak, S.-M.; Wu, Y.; Wu, Z.; Tian, Y.; Xiong, X.; Li, Y.; Liu, W.; Siahrostami, S.; Kuang, Y.; Yang, X.-Q.; Duan, H.; Feng, Z.; Wang, H.; Sun, X. Introducing Fe2+ into Nickel—Iron Layered Double Hydroxide: Local Structure Modulated Water Oxidation Activity. *Angew. Chem., Int. Ed.* **2018**, *57*, 9392—9396.
- (56) Grosvenor, A. P.; Kobe, B. A.; Biesinger, M. C.; McIntyre, N. S. Investigation of Multiplet Splitting of Fe 2p XPS Spectra and Bonding in Iron Compounds. *Surf. Interface Anal.* **2004**, *36*, 1564–1574.
- (57) Wang, B.; Zhao, K.; Yu, Z.; Sun, C.; Wang, Z.; Feng, N.; Mai, L.; Wang, Y.; Xia, Y. In Situ Structural Evolution of the Multi-Site Alloy Electrocatalyst to Manipulate the Intermediate for Enhanced Water Oxidation Reaction. *Energy Environ. Sci.* **2020**, *13*, 2200–2208.
- (58) Wu, X. J.; Zhang, Z. Z.; Liang, Q. S.; Meng, J. Evolution from (110) Fe to (111) Fe3O4 Thin Films Grown by Magnetron Sputtering Using Fe2O3 Target. *J. Cryst. Growth* **2012**, 340, 74–77.
- (59) Trotochaud, L.; Young, S. L.; Ranney, J. K.; Boettcher, S. W. Nickel–Iron Oxyhydroxide Oxygen-Evolution Electrocatalysts: The Role of Intentional and Incidental Iron Incorporation. *J. Am. Chem. Soc.* **2014**, *136*, 6744–6753.
- (60) Qiu, Z.; Tai, C.-W.; Niklasson, G. A.; Edvinsson, T. Direct Observation of Active Catalyst Surface Phases and the Effect of Dynamic Self-Optimization in NiFe-Layered Double Hydroxides for Alkaline Water Splitting. *Energy Environ. Sci.* **2019**, *12*, 572–581.
- (61) Wang, R.; Xu, C.; Lee, J.-M. High Performance Asymmetric Supercapacitors: New NiOOH Nanosheet/Graphene Hydrogels and Pure Graphene Hydrogels. *Nano Energy* **2016**, *19*, 210–221.
- (62) Yamashita, T.; Hayes, P. Analysis of XPS Spectra of Fe2+ and Fe3+ Ions in Oxide Materials. *Appl. Surf. Sci.* **2008**, 254, 2441–2449.
- (63) Heese-Gärtlein, J.; Rabe, A.; Behrens, M. Challenges in the Application of Manganese Oxide Powders as OER Electrocatalysts: Synthesis, Characterization, Activity and Stability of Nine Different MnxOy Compounds. Z. Anorg. Allg. Chem. 2021, 647, 1363–1372.
- (64) Liu, T.; Ma, X.; Liu, D.; Hao, S.; Du, G.; Ma, Y.; Asiri, A. M.; Sun, X.; Chen, L. Mn Doping of CoP Nanosheets Array: An Efficient Electrocatalyst for Hydrogen Evolution Reaction with Enhanced Activity at All PH Values. *ACS Catal.* **2017**, *7*, 98–102.
- (65) Xu, X.; Liang, H.; Tang, G.; Hong, Y.; Xie, Y.; Qi, Z.; Xu, B.; Wang, Z. Accelerating the Water Splitting Kinetics of CoP Microcubes Anchored on a Graphene Electrocatalyst by Mn Incorporation. *Nanoscale Adv.* **2019**, *1*, 177–183.
- (66) Browne, M. P.; Urbanova, V.; Plutnar, J.; Novotný, F.; Pumera, M. Inherent Impurities in 3D-Printed Electrodes Are Responsible for Catalysis towards Water Splitting. *J. Mater. Chem. A* **2020**, *8*, 1120–1126.
- (67) Shin, H.-C.; Liu, M. Copper Foam Structures with Highly Porous Nanostructured Walls. *Chem. Mater.* **2004**, *16*, 5460–5464.
- (68) Chen, R.; Yang, C.; Cai, W.; Wang, H.-Y.; Miao, J.; Zhang, L.; Chen, S.; Liu, B. Use of Platinum as the Counter Electrode to Study the Activity of Nonprecious Metal Catalysts for the Hydrogen Evolution Reaction. ACS Energy Lett. 2017, 2, 1070—1075.

(69) Morales, D. M.; Risch, M. Seven Steps to Reliable Cyclic Voltammetry Measurements for the Determination of Double Layer Capacitance. J. Phys. Energy 2021, 3, No. 034013.

TRECOMMENDED Recommended by ACS

Glassy Carbon Substrate Oxidation Effects on Electrode Stability for Oxygen Evolution Reaction Catalysis Stability **Benchmarking**

Jane Edgington, Linsey C. Seitz, et al.

SEPTEMBER 19, 2022

ACS APPLIED ENERGY MATERIALS

READ 🗹

Dealloying-Derived Nanoporous Bismuth for Selective CO, **Electroreduction to Formate**

Qingru Wei, Zhonghua Zhang, et al.

SEPTEMBER 26, 2022

THE JOURNAL OF PHYSICAL CHEMISTRY LETTERS

READ 🗹

Enhanced Capillary Wicking through Hierarchically Porous Constructs Derived from Bijel Templates

Jonggyu Lee, Yoonjin Won, et al.

NOVEMBER 07, 2022

LANGMUIR

READ 🗹

Janus Membranes with Graphene Meshes and ZnO Rods for Controlling Dendritic Growth in High-Performance Li Metal **Anodes**

Dae Yeop Jeong, Won Il Park, et al.

MARCH 30, 2022

ACS APPLIED ENERGY MATERIALS

READ 🗹

Get More Suggestions >